Cerebral Cortex, 2022;32: 1840–1865

https://doi.org/10.1093/cercor/bhab315
Advance Access Publication Date: 17 September 2021
Original Article

ORIGINAL ARTICLE

Sublamina-Specific Dynamics and Ultrastructural Heterogeneity of Layer 6 Excitatory Synaptic Boutons in the Adult Human Temporal Lobe Neocortex

Sandra Schmuhl-Giesen[1,2,†], Astrid Rollenhagen[1], Bernd Walkenfort[3], Rachida Yakoubi[1], Kurt Sätzler[4], Dorothea Miller[5], Marec von Lehe[6], Mike Hasenberg[3] and Joachim HR Lübke[1,7,8]

[1]Institute of Neuroscience and Medicine INM-10, Research Centre Jülich GmbH, 52425, Jülich, Germany, [2]Medical Faculty/RWTH University Hospital Aachen, 52074, Aachen, Germany, [3]Imaging Center Essen (IMCES), Electron Microscopy Unit (EMU), Medical Faculty of the University of Duisburg-Essen, 45147, Essen, Germany, [4]School of Biomedical Sciences, University of Ulster, Londonderry, BT52 1SA, UK, [5]University Hospital/Knappschaftskrankenhaus Bochum, 44892, Bochum, Germany, [6]Department of Neurosurgery, Brandenburg Medical School, Ruppiner Clinics, 16816, Neuruppin, Germany, [7]Department of Psychiatry, Psychotherapy and Psychosomatics, Medical Faculty/RWTH University Hospital Aachen, 52074, Aachen, Germany and [8]JARA Translational Brain Medicine, 52425/52074, Jülich/Aachen, Germany

Address correspondence to Joachim Lübke, Institute of Neuroscience and Medicine INM-10, Research Centre Jülich GmbH, 52425 Jülich, Germany. Email: j.luebke@fz-juelich.de
[†]Current address: Department of Gynecology, Charité/University Hospital Berlin, Charitéplatz 1, 10117 Berlin, Germany

Abstract

Synapses "govern" the computational properties of any given network in the brain. However, their detailed quantitative morphology is still rather unknown, particularly in humans. Quantitative 3D-models of synaptic boutons (SBs) in layer (L)6a and L6b of the temporal lobe neocortex (TLN) were generated from biopsy samples after epilepsy surgery using fine-scale transmission electron microscopy, 3D-volume reconstructions and electron microscopic tomography. Beside the overall geometry of SBs, the size of active zones (AZs) and that of the three pools of synaptic vesicles (SVs) were quantified. SBs in L6 of the TLN were middle-sized (~5 μm^2), the majority contained only a single but comparatively large AZ (~0.20 μm^2). SBs had a total pool of ~1100 SVs with comparatively large readily releasable (RRP, ~10 SVs L6a), (RRP, ~15 SVs L6b), recycling (RP, ~150 SVs), and resting (~900 SVs) pools. All pools showed a remarkably large variability suggesting a strong modulation of short-term synaptic plasticity. In conclusion, L6 SBs are highly reliable in synaptic transmission within the L6 network in the TLN and may act as "amplifiers," "integrators" but also as "discriminators" for columnar specific, long-range extracortical and cortico-thalamic signals from the sensory periphery.

Key words: electron microscopic tomography, human temporal lobe neocortex, layer 6 synaptic boutons, quantitative 3D-models of synaptic boutons, transmission electron microscopy

Introduction

The temporal lobe neocortex (TLN) is located at the baso-lateral side of the cerebral hemispheres and can only be found in primates including humans. It occupies ~20% of the total volume of human cerebral cortex (Kiernan 2012) and is regarded as a highly specialized associative, homotypic granular, and six-layered neocortex (von Economo and Koskinas 1925; Vogt 2009; Zilles et al. 2015; Zilles and Palomero-Gallagher 2017). Beside various other functions, the TLN is involved in auditory, visual, vestibular, linguistic, and olfactory information processing. Beside connections to various other neocortical areas, the TLN is linked to other multimodal association areas like the limbic system. Hence, the TLN is regarded as a higher-order multimodal, but not primary, or early sensory neocortex (reviewed by Insausti 2013).

The growing interest in working on the TLN is its involvement in several neurological diseases; most importantly as the area of origin and onset of temporal lobe epilepsy, the most common form of epilepsy (reviewed by Allone et al. 2017; Tai et al. 2018).

Taken together, the TLN represents an important region in the normal and pathologically altered human brain.

In various animal species including non-human primates (NHPs) and humans, L6 is present in all neocortical regions and can be subdivided into two distinct sublaminae, L6a and L6b (Tömböl et al. 1975; Tomböl 1984; Zhang and Deschênes 1997, 1998; Mercer et al. 2005; Watakabe et al. 2007; Kumar and Ohana 2008; Andjelic et al. 2009; Chen et al. 2009; Rowell et al. 2010; reviewed by Briggs 2010; Thomson 2010). In sensory cortices, L6a receives afferents from the specific thalamic relay nuclei. In turn, a subpopulation of L6a pyramidal neurons project back to these nuclei hence forms an excitatory feedback loop allowing the direct control of their excitatory input. In addition, L6 is intracortically connected with L4 excitatory spiny stellate and star pyramidal cells and in turn receives direct input from this layer (Marx and Feldmeyer 2013; Qi and Feldmeyer 2016; Marx et al. 2017).

Hence, L6 represents an important layer for both thalamocortical and intracortical information processing within and across cortical columns (Zhang and Deschênes 1997, 1998; Hay et al. 2015; Frandolig et al. 2019; reviewed by Briggs 2010; Feldmeyer and Lübke, 2010; Thomson 2010; Feldmeyer 2012).

The neuronal composition and subdivision of L6 also reflects its dual origin. L6a is a derivate of the early cortical plate with cortico-thalamic and cortico-cortical projecting pyramidal neurons (Zhang and Deschênes 1997, 1998; Kumar and Ohana 2008; Marx and Feldmeyer 2013; Marx et al. 2017, Diao et al. 2018), whereas L6b is more heterogeneous with neurons originating from the transient "subplate" and primordial plexiform layer (Marx et al. 2017). In contrast to L6a, pyramidal neurons in L6b are highly diverse in their dendritic configuration, axonal arborizations and projection; beside normally oriented pyramidal neurons with vertically oriented apical dendrites like those in L6a, a substantial fraction are inverted, horizontally oriented or with two thick main apical trunks (Tömböl et al. 1975; Tömböl 1984; Miller 1988; Andjelic et al. 2009; Chen et al. 2009; reviewed by Briggs 2010; Feldmeyer and Lübke 2010; Thomson 2010).

In contrast to its neuronal composition, relatively little is known about the synaptic organization of L6, in particular the quantitative geometry of SBs and their target structures in both sublaminae, at least in the human TLN. Moreover, whether the neuronal composition and dual origin of the two sublaminae is also reflected in the structural composition of SBs and their density remains unknown.

To fill this gap, biopsy samples of non-affected (non-epileptic) neocortical access tissue of the temporal lobe (TL) from patients that had to undergo amygdalo-hippocampectomy was used to investigate the layer-specific morphology and differences of L6 SBs. Using high-end fine-scale transmission electron microscopy (TEM) and 3D-volume reconstructions, quantitative 3D-models of excitatory synapses in L6a and L6b were generated. In particular, structural parameters that represent morphological correlates of synaptic transmission and plasticity were quantified such as the number, size and shape of AZs and that of the three pools of SVs, namely the readily releasable (RRP), the recycling (RP), and resting pool and compared with values obtained from already investigated layers of the TLN (Yakoubi et al. 2019a, 2019b) and data from experimental animals where available.

Here, we demonstrate layer-specific differences in the quantitative morphology of SBs, in particular for the shape and size of AZs, and most importantly for the size of the RRP, RP, and resting pools. No significant sublaminar-specific differences in the quantitative morphology of SBs were found, despite the size of the RRP and the large variability of structural and synaptic parameters investigated.

In conclusion, L6 SBs can be regarded as highly reliable in synaptic transmission and may act as "amplifiers," "integrators" but also as "discriminators" for columnar specific, long-range extracortical and cortico-thalamic signals from the sensory periphery within the L6 network.

Material and Methods

All experimental procedures were approved by the Ethical Committees of the Rheinische Friedrich-Wilhelms-University/ University Hospital Bonn (Ethic Votum of the Medical Faculty to Prof. Dr med. Johannes Schramm and Prof. Dr rer. nat. Joachim Lübke, Nr. 146/11), and the University of Bochum (Ethic Votum of the Medical Faculty to PD Dr med. Marec von Lehe and Prof. Dr rer. nat. Joachim Lübke, Reg. No. 5190-14-15; Ethic Votum of the Medical Faculty to Dr med. Dorothea Miller and Prof. Dr rer. nat. Joachim Lübke, Reg. No. 17-6199-BR), and the EU directive (2015/565/EC and 2015/566/EC) concerning the work with human tissue samples. The consent of the patients was obtained by written and signed statements for all experiments.

Tissue Extraction and Fixation

The adult human neocortical brain tissue was taken from the superior, medial, and inferior TL from four patients, ranging from 25 to 63 years in age that suffered from drug-resistant TLE (see Supplementary Table 1) and therefore had to undergo a transcortical selective amygdalo-hippocampectomy. The neocortical access tissue was considered as non-affected (non-epileptic) since it was always located far from the epileptic focus as routinely monitored by preoperative electrophysiology and magnetic resonance imaging. The "normality" of such neocortical access tissue has also been demonstrated by other recent structural and functional studies using the same experimental approach (Testa-Silva et al. 2014; Mohan et al. 2015; Molnár et al. 2016; Seeman et al. 2018; Yakoubi et al. 2019a, 2019b; reviewed by Mansfelder et al. 2019).

During epilepsy surgery, tissue from the three temporal gyri was transected to access the hippocampus via a transcortical, transventricular pathway. After removal, the extracted tissue samples were immediately immersion-fixed in fresh ice-cold 4% paraformaldehyde and 2.5% glutaraldehyde diluted in 0.1 M phosphate buffer (PB, pH 7.4) and incubated 24–72 h at 4°C. Four hours after removal of the tissue samples, the fixative was replaced by the same, but fresh solution. Prior to vibratome sectioning, tissue samples were thoroughly rinsed in cold PB and afterwards embedded in 5% Agar-Agar (Sigma) diluted in PB. Tissue blocks were cut in the coronal plane through the TLN with a Vibratome VT 1000S (Leica Microsystems GmbH) into 150–200-μm thick sections. Afterwards they were thoroughly washed again in PB and transferred to 0.5–1% PB-sucrose buffered OsO_4 (300 mOsm, pH 7.4; Sigma) for 60–90 min. After visual inspection, sections were washed several times in PB and left overnight at 4°C. The next day, sections were dehydrated with an ascending series of ethanol starting at 20%, 30%, 50%, 60%, 70%, 80%, and 90% (15 min for each step), followed by 95% ethanol (20 min) and finally in 100% ethanol (twice 30 min). Subsequently sections were transferred briefly into propylene oxide (twice 2 min) and then incubated in a mixture of propylene oxide and Durcupan (2:1 and 1:1, 60 min for each step; Fa. Fluka) and stored in pure Durcupan overnight at room temperature. Finally, sections were flat-embedded in fresh Durcupan between Acla foils and polymerized at 60°C for 48 h.

Semi- and Ultrathin Sectioning

Embedded tissue samples of the TLN were inspected light microscopically to determine the region of interest (ROI), which was then trimmed out and glued onto a pre-polymerized block. To look for the quality (preservation of the tissue) and to define the final ROI, in this case layer 6a and L6b of the TLN, semithin sections were cut using a Histo-diamond knife (Fa. Diatome, Nidau) with a Leica UltracutS ultramicrotome (Leica Microsystems) and stained with methylene-blue (see also Supplementary Fig. 1). After inspection and definition of the final ROI in either L6a and L6b, the block was further trimmed to its final size for serial ultrathin sectioning. In methylene-blue stained semithin sections, L6a and L6b were identified as the area under the large L5 pyramidal neurons (L6a) and the area above the white matter (L6b; see also Supplementary Fig. 1).

Serial ultrathin sections (50 ± 5 nm in thickness; silver to gray interference contrast) were cut with the same Leica UltracutS and collected on pioloform-coated slot copper grids (Fa. Plano). An individual series comprised usually between 75 and 150 ultrathin sections to reconstruct SBs of different shape and size to meet both structural variability and statistical variance. Prior to electron micrography (EM) examination and to increase the contrast, ultrathin sections were finally stained with 5% aqueous uranyl acetate for 15–20 min and lead citrate for 3–5 min.

EM Data Acquisition

Ultrathin sections were examined with a Zeiss Libra 120 TEM (Fa. Zeiss) equipped with a bottom-mounted Proscan 2K digital camera using the Image SP software (Fa. Tröndle) at a magnification of 8000× with frames of 6 × 6 images (10 444 × 11 129 final pixel size). After the definition of 1–3 different ROIs in either L6a or L6b they were photographed throughout consecutive sections in the entire series of ultrathin sections. Afterwards all images were stored in a database until further processing. Additional photographs of interesting structural elements in L6a and L6b were taken at different magnifications to describe characteristic features of SBs, their target structures and other interesting subelements in the neuronal network of L6. Selected EM images were further edited for publication using the Adobe Photoshop and Adobe Illustrator software.

3D-Volume Reconstructions of SBs and Their Target Structures

Serial EM images were then imported, stacked and aligned in OpenCAR (Contour Alignment Reconstruction; for details see Sätzler et al. 2002). Afterwards, a series was then inspected for SBs that can be followed from the beginning to their end. An SB was considered completely captured, when it was possible to follow the axon in both directions until the occurrence (swelling) of a SB (*en passant* boutons) or the enlargement of the axon leading to an endterminal bouton. The start of a bouton was defined by the typical widening of the axon and the abrupt occurrence of SVs. All synaptic structures of interest were outlined on the outer edge of their membranes throughout the series of EM images.

3D-volume reconstructions were then generated and the following structural parameters were analyzed: 1) surface area and volume of SBs; 2) volume of mitochondria; 3) surface area of the presynaptic active zones (PreAZs) and postsynaptic densities (PSDs); 4) number and diameter of clear synaptic and dense core vesicles (DCVs); and 5) total pool of SVs and the RRP, RP, and resting pool.

Excitatory SBs in L6a and L6b were characterized by large round SVs and prominent PreAZs and PSDs in contrast to putative GABAergic terminals that had smaller, more oval-shaped SVs and thin or no prominent PSDs.

The PreAZs and PSDs were regarded as complete when their perimeters were entirely reconstructed in a series of EM images. Per definition, the PreAZ and PSD constituting the AZ are regions of densely, electron-dense, dark-appearing material, and condensed at the pre- and postsynaptic apposition zone. The surface areas of the PreAZ and PSD were computed separately by first generating a 3D surface model of the SB. The PreAZ was then measured by extracting this area from the reconstructed presynaptic bouton membrane that was covered by this membrane specialization (i.e., where the contour line coincided with $<$30 nm distance from the presynaptic membrane). Hence, the length (l) of the PreAZ (l PreAZ) and the surface area (SA) of the PreAZ (SA PreAZ) is already known. The size of the PSD opposing the PreAZ was estimated under the following assumptions: 1) both membrane specializations, PreAZ and PSD run parallel to each other at the pre- and postsynaptic apposition zone; and 2) for both membrane specializations a contour line was drawn determining their actual length (l PreAZ and l PSD). Hence, the surface area of the PSD (SA PSD) is estimated by the following equation:

$$\text{SA PSD} = \text{SA Pre} * \text{l PSD}/\text{l PreAZ}$$

which is the perimeter ratio between the outlines of the PSD to that of the synaptic contact.

The synaptic cleft diameter was measured because of its importance for the transient increase of the glutamate concentration, reversible binding of glutamate to appropriate glutamate receptors and eventual uptake and diffusion of glutamate out of the cleft by fine astrocytic processes. To a large extent these

processes are governed by the geometry of the synaptic cleft and the shape and size of the PreAZs and PSDs. Synaptic cleft width measurement was performed only on synaptic contacts cut perpendicular to the AZ and showed the typical broadening of the synaptic cleft ($n = 4$ patients, $n = 120$ AZs). The distance between the outer edge of the pre- and postsynaptic membranes at the center of the synaptic contact and at the two lateral edges was measured and averaged for each synaptic contact. The two values for the lateral edges were averaged and a mean ± standard deviation (SD) was calculated for each patient. Finally, a total mean ± SD over all patients was given.

All SVs were marked throughout each SB and their diameters (outer to outer membrane) were individually measured. To determine the distribution profile of the SVs, the minimal distance between each SV membrane to the contour lines of the PreAZ was measured throughout the SB in every single image of the series. Large DCVs were only counted in the image where they appeared largest (for details see Yakoubi et al. 2019a, 2019b).

Tissue Shrinkage

In this study aldehyde fixation was used that is thought to induce tissue shrinkage thereby biasing structural quantification (but see Korogod et al. 2015). A direct comparison of structural parameters obtained from either aldehyde or cryo-fixed and substituted tissue samples (Korogod et al. 2015) showed differences in cortical thickness (~16% larger in cryro-fixed material), volume of extracellular space (~6-fold larger in cryo-fixed material), and a slight increase in glial volume.

Concerning synaptic parameters as estimated here, no significant differences were found for SB size and other synaptic subelements such as mitochondria, AZs and SVs (Zhao et al. 2012a, 2012b; Korogod et al. 2015). Therefore, no correction for shrinkage was applied and we are thus convinced that the synaptic parameters reported here are accurate and can be directly used for detailed computational models. In addition, large-scale preservation for ultrastructural analysis will therefore continue to rely on chemical fixation approaches, due to the limited preservation of the ultrastructure in cryo-fixed material as stated in Korogod et al. (2015).

EM Tomography of L6 SBs in the TLN

EM tomography was carried out on 200–300-nm thick sections cut from L6 containing blocks prepared for ultrathin sectioning as described above. For the analysis of L6, two patients were used and the analysis was carried out on four tomography prepared sections for L6a and L6b, respectively. In addition, and for comparison with L4, tomography prepared sections from two series of one patient were imaged and analyzed. Sections were mounted on either pioloform-coated line or slot copper grids (Plano) and were counterstained with uranyl acetate and lead citrate (see above). Subsequently, sections were examined with a JEOL JEM 1400Plus, operating at 120 kV and equipped with a 4096 × 4096 pixels CMOS camera (TemCam-F416, TVIPS). Tilt series were acquired automatically over an angular range of −60° to +60° at 1° increments using Serial EM (Ver. 3.58; Mastronarde 2005). Stack alignment and reconstruction by filtered back-projection were carried out using the software package iMOD (Ver. 4.9.7; Kremer et al. 1996). Final reconstructions were ultimately filtered using a median filter with a window size of three pixels. In individual tilt series through SBs in L6a and L6b (Table 4) "docked" vesicles were counted separately for spine and shaft SBs. For comparison, additional L4 SBs were analyzed the same way.

Cluster Analysis of L6 Excitatory SBs in the Human TLN

The excitatory SBs of L6 in the human TLN showed a large variability in both their shape and size in most structural parameters investigated, which already indicate the presence of several types of SBs within our sample. Therefore, to determine the most characteristic features that best identify the different groups that is, types of SBs, a cluster analysis (CA) was performed on excitatory SBs of L6a ($n = 95$) and L6b ($n = 85$) using MATLAB and Statistics Toolbox Release 2016b (The MathWorks, Inc.) based on the following structural parameters: volume, surface area and sphericity of SBs, number of AZs/SB, PreAZ and PSD surface area, number and volume of mitochondria/SB, percentage of mitochondrial volume to the total SB volume, total number of SVs/SB, total vesicular volume/SB and its percentage to the total SB volume, SV diameter, and number of SVs at different perimeters 10/20/30/40/60/70/80/90/100/200/300/400/500 nm from the PreAZs, and finally the total number of DCVs/SB.

First, zero-mean normalization was applied as the parameters had different units. Then, a principal component analysis (PCA) was performed on the original dataset to simplify it, by applying a rank reduction, to a smaller dataset of linearly uncorrelated variables called principal components (PCs), but still containing most of the information of the original dataset. The PCA allows the detection of the main features that best characterized the excitatory SBs of L6a and L6b and thus showed that the first PC was predominantly defined by the surface area of the PreAZs and PSDs as well as the vesicle pools at different perimeters from the PreAZs. Subsequently, the simplified dataset was used to perform a hierarchical cluster analysis (HCA) a method for unsupervised learning, since the original dataset was not labeled (for further details see Yakoubi et al. 2019a).

Golgi-Cox Impregnation of Biopsy Material

Three human tissue blocks from the medial and inferior gyrus of the TLN were processed with the Golgi-Cox impregnation technique using the commercially available Hito Golgi-Cox OptimStain kit (Hitobiotec Corp). After removal of the biopsy samples, tissue was briefly rinsed twice in double distilled water (dd H_2O), and then transferred into the impregnation solution overnight at room temperature. The next day, samples were incubated in a fresh impregnation solution and stored for 14 days in the dark at room temperature. Samples were then transferred in solution 3 in the dark at room temperature for 1 day. Thereafter, they were placed into fresh solution 3 in the dark at room temperature for six additional days. Then, solution 3 was exchanged and samples were stored at 4°C in the dark overnight. Tissue blocks were embedded in 5% Agarose (Carl Roth) diluted in dd H_2O, and sectioned with a vibratome in the coronal plane at 100–250 μm thickness and then transferred to dd H_2O. After careful removal of the agarose, free-floating sections were incubated into solution 3 for 2–3 min in the dark at room temperature, and right after placed into dd H_2O, washed several times, and stored overnight. The next day, sections were put into a mixture of solutions 4 and 5 for 10 min at room temperature. Afterwards, they were rinsed twice in dd H_2O for 4 min each, dehydrated in 50%, 70%, and 95% ethanol for 5 min each, then transferred into absolute ethanol (3 × 5 min), defatted in xylene, and finally

embedded in Eukitt (Sigma-Aldrich) coverslipped and air-dried. Finally, sections were examined and imaged with an Olympus BX 61 light microscope equipped with the CellSense software package (Olympus). For publication, selected images were further processed using Adobe Photoshop and Adobe Illustrator.

Measurement of the Synaptic Density

In order to examine and further analyze structural parameters that allow more detailed information in functionality and plasticity within the human brain (DeFelipe et al. 1999; Anton–Sanchez et al. 2014; Dominguez-Alvaro et al. 2019), a stereological unbiased estimation of the density of synaptic contacts was performed using a physical dissector technique (Mayhew 1996; Fiala and Harris 2001; Yakoubi et al. 2019b). For this analysis, the same series of ultrathin sections was used as for the 3D-reconstructions. To calculate the synaptic density for each patient and sublamina, L6a and L6b, a stack of 20 successive frames (also called dissector) within each series was cutout, aligned and edited with Fiji ImageJ (Schindelin et al. 2012; https://fiji.sc). A grid was layered over each image and newly emerged synapses were marked and counted by using the previous section as a reference to avoid double counting. The results have then been inserted in the following formula (Fiala and Harris 2001):

$$\mathrm{Nv} = \frac{\sum d\,\mathrm{Qd}}{\sum d\,\mathrm{Vd}}$$

In this case, Nv is the density of synaptic contacts in a virtual volume calculated for the number of synaptic contacts per volume, Q_d is the number of synaptic contacts per dissector and V_d is the volume of the dissector given by the number of dissectors × frame area × section thickness.

Quantitative Analysis of the Astrocytic Coverage

To quantify the astrocytic coverage of synaptic complexes that constitute the "tripartite" synapse in the human neocortex, the interactive software ImageJ (Schneider et al. 2012) was used. The first, the middle, and the last images of a series were used for a further quantitative volumetric analysis. In each section of the same series used for the 3D-volume reconstructions, a grid (grid size $0.8 \times 0.8\ \mu m^2$) was placed over the EM image, and in each square, the abundance of fine astrocytic processes was documented throughout these images and averaged. Using the Cavalieri method [Unbiased Stereology: Three-Dimensional Measurement in Microscopy (Advanced Methods) Paperback—7 January 2005 by Vyvyan Howard Matthew Reed], the (absolute) volume contribution of astrocytic processes was determined according to the Cavalieri estimator:

$$V = a(p) \times \Sigma P \times t$$

where $a(p)$ is the size of one square ($0.8 \times 0.8\ \mu m^2$), P is the number of squares counted, and t is the thickness of the slice.

Statistical Analysis

The mean value expressed as the total mean over single means for each patient ± SD, the median with the first and third quartile (interquartile range, IQR), the coefficient of correlation (R^2), the coefficient of variation (CV), skewness, the degree of asymmetry observed in a probability distribution, and the variance, a statistical measure of variability, was given for each structural parameter analyzed. The P-value was considered significant only if $P \leq 0.05$. Box- and Violin plots were generated to investigate interindividual and age-dependent differences for each patient and structural parameter (Ploty 4.0.0 https://chart-studio.ploty.com; see Supplementary Figs 2 and 3 and Supplementary Table 1). In addition, synaptic density measurements were statistically tested for interindividual and age-dependent differences. For statistical comparison data obtained for L5 ($n = 7$ patients ranging from 20 to 50 in age; Yakoubi et al. 2019a) and L4 ($n = 6$ patients ranging from 25 to 63 in age; Yakoubi et al. 2019b) were included in the present study (see Supplementary Tables 1 and 2).

To test for significant differences between both subjects and layers the non-parametric Kruskal–Wallis H-test analysis was computed, using PAST 4.02 (Hammer et al. 2001), as some of the analyzed parameters were not normally distributed as indicated by the skewness.

Correlation graphs between several structural parameters were generated. The R^2 values were interpreted as follows: 0, no linear correlation; 0–0.5, weak linear correlation; 0.5–0.8, good linear correlation; and 0.8–1.0, strong linear correlation. Furthermore, a freely available Fisher's r-to-z-transformation calculator was used to test for difference in R^2 between L6a and L6b (P value ≤ 0.05).

Results

Synaptic Density in L6 of the Human TLN

The density of synaptic contacts in L6a and L6b was estimated from the same series of ultrathin sections used for the quantitative 3D-volume reconstructions ($n = 4$ patients ranging from 25 to 63 years in age). For comparison, data in L4 from 6 patients ranging from 24 to 63 in age were taken from Yakoubi et al. (2019b; see Material and Methods; and Supplementary Table 1) because both layers are main recipients of thalamo-cortical afferents (reviewed by Sherman 2012). These measurements provide the basis to further gain information regarding the synaptic organization of the neuropil, rate of connectivity as well as possible interindividual differences in the human TLN.

In L6, the overall density was 4.98×10^7 synapses/mm^3, ranging from 2.6×10^7 to 7.3×10^7/mm^3, but the averaged synaptic density of L6a versus L6b showed a ~1.5-fold difference. Strikingly, also a huge interindividual variability was found, although with no significant differences between individuals, ages and L6a versus L6b. However, a significant difference in synaptic density by ~20-fold ($P \leq 0.01$) was observed between L6 and L4 (Table 1).

In all patients, the majority of synaptic contacts counted were excitatory and were found predominantly on spines (L6a: 81%; L6b: 79%) of different types (Table 1). The remainder contacts were established on dendritic shafts (L6a: 29%; L6b: 21%). Interestingly, no significant difference in the innervation of target structures (dendritic shafts vs., dendritic spines) between L6a, L6b, and L4 was found, respectively. Finally, the majority of spines in both sublaminae contained a spine apparatus (~90%) with no significant differences between both sublaminae, but strikingly different by ~20-fold when compared with data obtained in L4 of the human TLN (~40%; Yakoubi et al. 2019b).

In summary, the synaptic density in L6 of the TLN was strikingly by ~20-fold higher than in L4, indicating a lamina-specific difference in synaptic density (see Discussion) but may

Table 1 Density of synaptic contacts in L6a, L6b, and L4 of the human TLN

Patients	L6a Hu_01	L6a Hu_02	L6a Hu_04	Mean L6a ± SD	L6b Hu_01	L6b Hu_02	L6b Hu_03	Mean L6b ± SD	Total mean L6 ± SD	Total mean L4 ± SD
Total density of synaptic contacts/mm^3	6.9×10^7	7.3×10^7	3.9×10^7	$6.03 \times 10^7 \pm 1.86 \times 10^7$	3.9×10^7	2.6×10^7	5.3×10^7	$3.93 \times 10^7 \pm 1.35 \times 10^7$ n.s.	$4.98 \times 10^7 \pm 1.85 \times 10^7$	$2.37 \times 10^6 \pm 2.19 \times 10^{6**}$
SBs on dendritic shafts (%)	18	7	32	19.00 ± 12.53	33	16	14	21.00 ± 10.44 n.s.	20.00 ± 10.37	20.34 ± 17.75 n.s.
SBs on dendritic spines (%)	82	93	68	81.00 ± 12.53	67	84	86	79.00 ± 10.44 n.s.	80.00 ± 10.37	76.62 ± 18.75 n.s.
Stubby spines (%)	20	7	7	11.33 ± 7.51	5	5	16	8.67 ± 8.35 n.s.	10.00 ± 6.39	3.50
Mushroom spines (%)	75	93	80	82.67 ± 9.29	85	67	56	69.33 ± 14.64 n.s.	76.00 ± 13.16	7.80
Elongated filopodial spines (%)	5	0	13	6.00 ± 6.56	10	28	28	22.00 ± 10.39 n.s.	14.00 ± 11.71	63.90
SBs with spine apparatus (%)	100	89	87	92.00 ± 7.00	75	100	94	89.67 ± 13.05 n.s.	90.83 ± 9.45	40.00

Note: ** $P \leq 0.01$; n.s. non-significant and not non-significant. Values are given as mean ± SD or percentage (%).

also suggest a high connectivity rate of neurons in L6 in the human TLN.

Neural Organization of the Human TLN

In Golgi-stained material (Fig. 1) and semithin sections (see Supplementary Fig. 1) taken from samples of the superior, medial and inferior gyrus of the human TLN (Fig. 1A,B, see Supplementary Fig. 1A). L6 can be distinguished and separated from L5, characterized by its large pyramidal cells, by the occurrence of smaller-sized pyramidal neurons (Fig. 1B,C). This is followed by a zone relatively sparse of neurons (Fig. 1B) that can be distinguished from the white mater by the rapid increase of myelinated axons and astrocytes (Figs 1B and 2A,B). Like in rodents and NHPs, L6 can be clearly subdivided in two distinct sublaminae, L6a and L6b according to their dual origin (see Introduction) and the steady increase in myelinated axons (compare Fig. 2A with 2B). In the human TLN, both sublaminae are nearly similar in size (Fig. 1B) throughout the entire TL and are mainly composed of excitatory pyramidal neurons of different shape and size (Figs 1B–D and 2A1,B1) and a heterogeneous population of GABAergic interneurons (Fig. 1C). In both sublaminae, pyramidal neurons are often organized in clusters (see Supplementary Fig. 1B–D).

L6a is mainly composed of pyramidal neurons characterized by a thick ascending, vertically oriented apical dendrite (Fig. 1B,C, see Supplementary Fig. 1C) equivalent to cortico-cortical and cortico-thalamic projecting pyramidal neurons described in rodents (Tomböl et al. 1975; Tomböl 1984; Zhang and Deschênnes 1997, 1998; Kumar and Ohana 2008; Marx and Feldmeyer 2013; Marx et al. 2017). In contrast, the population of pyramidal cells in L6b was very heterogenous with inverted (Figs 1B,D and 2B1, see Supplementary Fig. 1), horizontally or bipolar oriented pyramidal neurons with long apical dendrites (Fig. 1B,E, see Supplementary Fig. 1E) as also described in rodents (Tömböl et al. 1975; Tomböl 1984; Marx and Feldmeyer 2013). Most neurons, regardless whether they are excitatory or inhibitory contained so-called lipofuscin granula (Fig. 2A2), indicative for aging. In addition, lipofuscin granula were also observed in numerous astrocytes (not shown).

Interestingly, also degenerating apoptotic neurons were found as identified by their dark appearance characterized by severe distortions of their cytoplasm, large vacuoles and sometimes accompanied by microglia, indicative of cell death of these neurons in our biopsy samples in semi- and ultrathin sections (see Supplementary Figs 1D and 4A). In addition, dendrites in different stages of degeneration were observed that sometimes still receive synaptic input (see Supplementary Fig. 4B). However, their density varied substantially within our neocortical TL tissue samples.

Synaptic Organization of L6 in the Human TLN

The main goal of this study was to quantify morphological parameters representing structural correlates of synaptic transmission and plasticity in L6 excitatory SBs in the human TLN, separated for both sublaminae L6a and L6b. For this purpose, a total of 182 SBs were completely reconstructed out of six series of 100–150 ultrathin sections/series. In L6a in three series 96 SBs and 97AZs and in L6b in three series 86 SBs and 84 AZs were quantified using non-affected (non-epileptic) neocortical access tissue from biopsies taken during epilepsy surgery (see Material and Methods; and Supplementary Table 1).

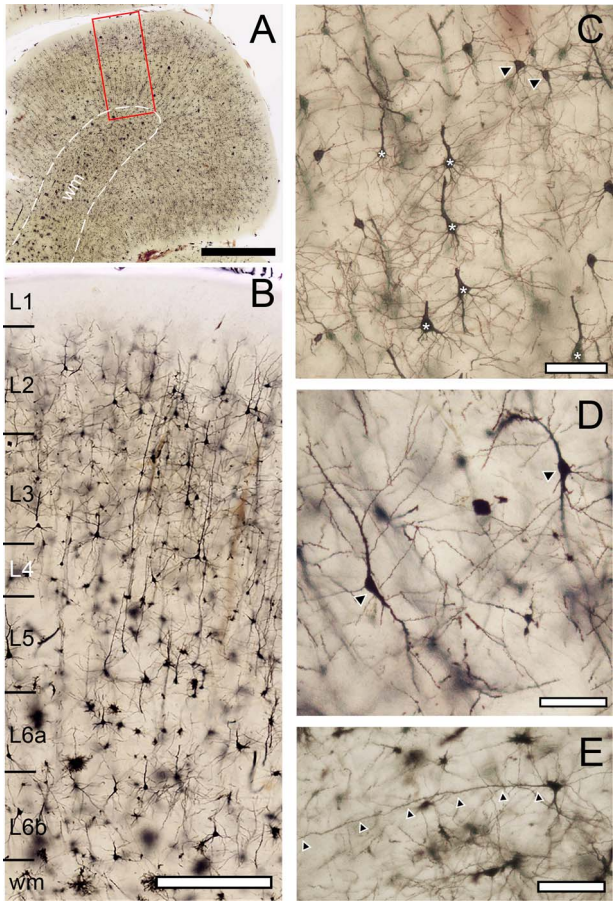

Figure 1. Neuronal organization of the human TLN and L6 as visualized by Golgi-staining. (*A*) Low power light micrograph through a Golgi-stained vibratome section of the human Gyrus temporalis medialis. Dashed lines indicate the border between the gray and white matter (wm). The framed area in red is shown at higher magnification in (*B*). Scale bar 2 mm. (*B*) Vertical slab through a cortical column in the human TLN showing the density and distribution of Golgi-stained neurons throughout all cortical layers (L1–L6). Note the high density of pyramidal neurons of different shape and size in L2 and L3 often with a terminal tuft dendrite in L1. In L4, L5, and L6 an abrupt change in the density of neurons is observed, which is comparatively lower than that in L2 and L3. Scale bar 500 μm. (*C*) Golgi-stained neurons in L6a. Pyramidal neurons (asterisks) are always identifiable by their characteristic shape and size of their somata and vertical orientation of their apical dendrites. Pyramidal cells are intermingled by a heterogenous population of GABAergic interneurons two of which are marked by arrowheads. (*D*) Two representative examples of bipolar tufted pyramidal neurons in L6b as identified by their two thick dendrites one ascending towards the pial surface the other oriented towards the white matter. (*E*) Typical example of a horizontally oriented pyramidal neuron with a prominent apical dendrite (marked by arrowheads) running parallel within L6b. Scale bar in *C*–*E* 100 μm.

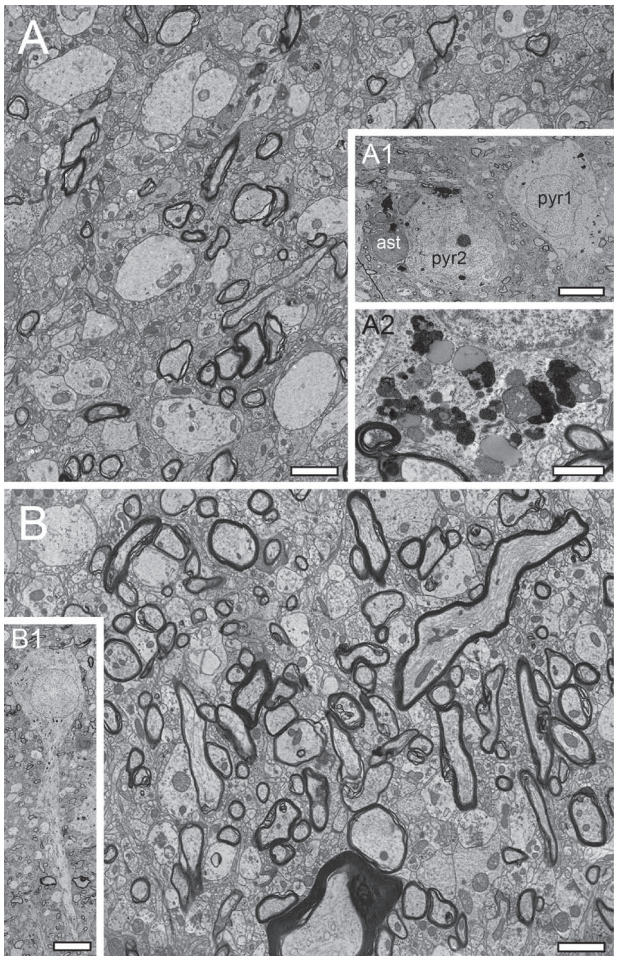

Figure 2. Neuronal organization of L6 in the human TLN. (*A*) Low power electron micrograph of the neuropil in L6a composed of dendritic and synaptic profiles of different shape and size. Layer 6a also contains numerous myelinated axons often accompanied by clusters of unmyelinated ones. Scale bar 1 μm. Inset *A1*: Two putative L6 pyramidal cell somata (pyr1, pyr2) identified by their large somata and nuclei and organization of their cytoplasm. Pyramidal cells (pyr2) are often accompanied by astrocytes (ast) identifiable by their darker appearance. Scale bar 25 μm. Inset *A2*: High magnification of lipofuscin granula in the cytoplasm of a pyramidal neuron a frequently found indicator of aging in these neurons. Scale bar 0.25 μm. (*B*) Typical example of the neuropil in L6b with a much higher density of myelinated axons ascending from the white matter when compared with L6a. Scale bar 1 um. Inset *B1*: Typical example of an inverted pyramidal neuron with a thick apical trunk descending towards the white matter. Scale bar 10 μm.

At the TEM level, L6 can be also distinguished from L5 by its smaller sized pyramidal neurons (L6a) and the abrupt increase in myelinated axons (Fig. 2A); their number steadily increased in L6b (Fig. 2B) towards the white matter.

In L6a and L6b the neuropil is composed of neuronal cell bodies often organized in cluster of 8–12 neurons (see Supplementary Fig. 1B–D), astrocytic cell bodies and their fine processes often associated with the neuronal clusters (Fig. 2A1, see Supplementary Fig. 1B–D), apical and basal dendrites of L6a and L6b neurons, and SBs of different shape and size (Figs 3 and 4). When organized in clusters, neurons in L6 were sometimes interconnected via gap-junctions (not shown).

Synaptic complexes in L6a und L6b were formed by either presynaptic *en passant* or endterminal boutons (Figs 3 and 4), with their prospective postsynaptic target structures, either a cell body of a neuron (not shown), or dendritic shafts (Figs 3A,C,G and 4E,H) or spines of different caliber (Figs 3A,B,D–F,H and 4A–D,F,G).

In both sublaminae, SBs were predominantly found on dendritic spines (86.00% in L6a and 72.73% in L6b), the remainder were located on dendritic shafts (Figs 3A,C,G and 4E,H; see also Table 1). Spines were classified according to established criteria (see for example: Gray 1959; Boyer et al. 1998; Holtmaat et al. 2005; Tamada et al. 2020). SBs on spines were predominantly located on mushroom spines with a variable length of the spine neck (66.00% in L6a and 55.84% in L6b), a smaller

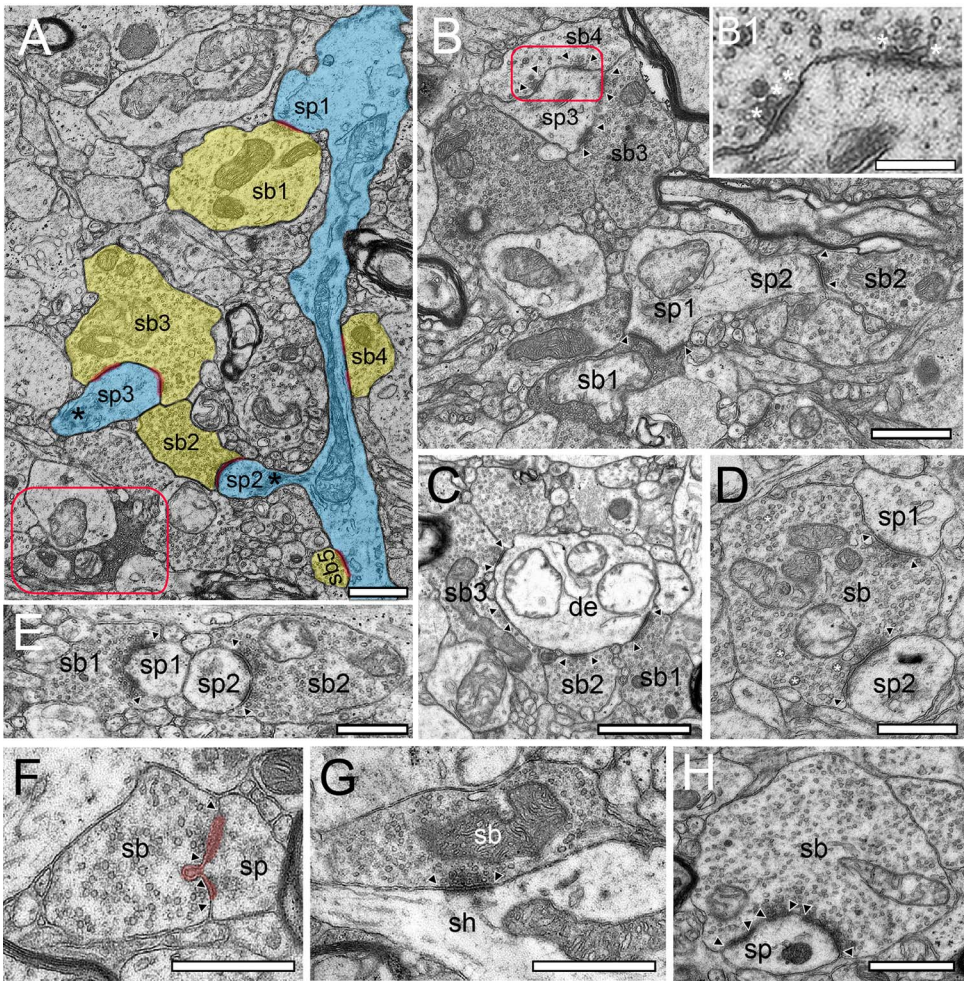

Figure 3. Synaptic boutons and their target structures in L6 of the human TLN. (*A*) Electron micrograph with several synaptic complexes in L6a. Here, synaptic boutons (sb) are always highlighted in transparent yellow, their respective target structures in transparent blue and AZs in transparent red. The dendritic segment (de) on the right receives synaptic input at a stubby spine (sp1, sb1), a mushroom spine (sp2, sb2) and two putative GABAergic shaft synapses (sb4, sb5) one of which (sb4) had two AZs. Close to the dendrite, a synaptic bouton (sb3) terminate directly on a large spine head (sp3) with two AZs. Note also the prominent spine apparatus in sp2 and sp3 marked by asterisks. The framed area shows a large astrocytic process containing gliotransmitter. Scale bar 0.5 μm. (*B*) Two large synaptic boutons (sb1, sb2) terminating on two opposite stubby spines (sp1, sp2) on a dendritic segment in L6b with two macular, non-perforated AZs spanning the entire pre- and postsynaptic apposition zone (arrowheads). A different spine (sp3) is innervated by a large glutamatergic synaptic bouton (sb3) with two AZs and a putative GABAergic bouton (sb4). The AZ of this bouton (frame area) is shown at higher magnification to demonstrate several fused or "docked" synaptic vesicles (marked by asterisks) in the inset *B1*. Scale bar in *B* 0.5 μm and *B1* 0.25 μm, respectively. (*C*) Dense innervation of a small caliber dendrite (de) in L6a by three excitatory synaptic boutons (sb1–sb3). The AZs are marked by arrowheads. Scale bar 1 μm. (*D*) Comparatively large synaptic bouton (sb) in L6b containing several mitochondria that establish synaptic contacts with two dendritic spines (sp1, sp2) one (sp2) with a relatively large macular, non-perforated AZ. Scale bar 0.5 μm. (*E*) Two twinned dendritic spines (sp1, sp2) emerging from the same dendrite in L6a receiving input from two synaptic boutons (sb1, sb2) both with perforated AZs (arrowheads). Scale bar 0.5 μm. (*F*) Large synaptic bouton (sb) terminating on a dendritic spine (sp) in L6b. Note the enfolding of the pre- and postsynaptic membranes at the AZ into the SB highlighted in transparent red. Scale bar 0.5 μm. (*G*) Large putative GABAergic endterminal bouton in L6b identified by its content of small ovoid synaptic vesicles and the small AZ (arrowheads) located on a dendritic shaft (sh). Sale bar 0.5 μm. (*H*) Endterminal synaptic bouton terminating on the spine head of a small caliber dendritic spine containing a multivesicular body with three separated AZs (arrowheads) in L6b. Scale bar 0.5 μm.

fraction on stubby (13.00% in L6a and 3.90% in L6b), or on thin elongated spines (7.00% in L6a and 12.99% in L6b); the remainder 14.00% in L6a and 27.27% in L6b were not classifiable.

Numerous SBs in both sublaminae were seen to establish either two or three synaptic contacts on the same spine (Fig. 4*D*,*G*), or dendrite (Figs 3*A*,*C* and 4*E*,*H*), or different spines of the same dendritic segment (Figs 3*B*,*E* and 4*H*). Infrequently, GABAergic synapses, identified by the smaller more spherical SVs, and glutamatergic terminals were found on the same spine (Fig. 3*B*). Interestingly, ~92% (L6a) and ~89% (L6b) of spines contained a spine apparatus (Fig. 3*A*,*B1*,*D*), a specialized form of the endoplasmic reticulum, which is thought to increase spine motility and stabilize the pre- and postsynaptic apposition zone during signal transduction (reviewed by Knott and Holtmaat 2008).

In numerous SBs in both sublaminae, so-called DCVs were distributed throughout the presynaptic terminal (Figs 3*H* and 4*D*,*G*,*H*) although their number varied substantially between individual SBs. In a few cases, DCVs were observed to fuse with the PreAZ indicating that a subpopulation may be involved in the build-up of the AZ (not shown).

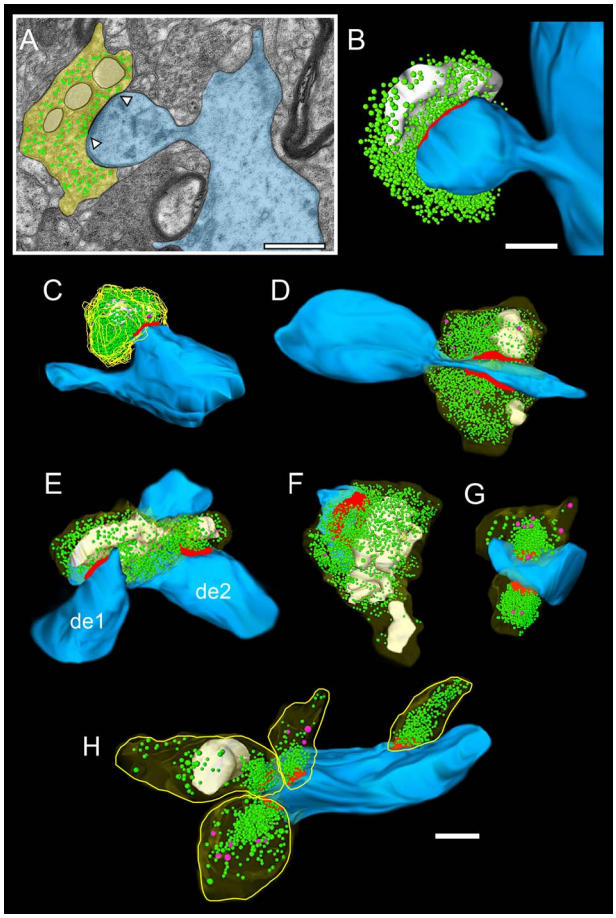

Figure 4. 3D-volume reconstructions of SBs in L6 of the human TLN. (*A*) Electron micrograph of a SB (sb) in L6a highlighted in transparent yellow terminating on a mushroom spine originating from a small caliber dendrite given in transparent blue. Presynaptic mitochondria are given in transparent white, SVs as green dots, DCVs as magenta dots, and the AZs is marked by arrowheads (*A*) or as a red contour in the subsequent 3D-volume reconstructions. Same color code as in A occur for all following panels. (*B*) 3D-volume reconstruction of the SB and its target spine shown in A reconstructed from serial ultrathin sections. Note the mitochondria associated with the pool of SVs (green dots) and the macular, non-perforated AZ (red). (*C*) SB terminating on a stubby spine in L6b. Here, the outline of the SB is given as contour lines to better allow the visualization of mitochondria, AZs, and synaptic vesicles. (*D*) Dendritic segment in L6a with an emerging elongated spine with two opposite SBs terminating on the beginning of the spine head with comparatively large AZs (red). Here, and in the following reconstructions SBs are made transparent yellow to visualize their content of structural subelements. (*E*) SB in L6b establishing two contacts on two different dendritic segments (de1, de2). (*F*) Large endterminal SB synapsing in L6a on a small caliber mushroom-shaped dendritic spine in L6b containing numerous mitochondria and a large macular AZ (red). (*G*) Two comparatively small caliber SBs in L6b terminating on a dendritic shaft lacking mitochondria but containing numerous DCVs. (*H*) Four SBs terminating on the dendritic shaft in L6b. Note the different geometry and size of the SBs, the pools of synaptic vesicles (green dots) and the content or lack of mitochondria. Scale bar in *A–H* 0.5 μm.

In addition, so-called clathrin-coated pits (not shown) were frequently observed in SBs of the human TLN, some of which are located near the AZ suggesting a role in membrane trafficking. Clathrin-coated vesicles are thought to selectively sort cargo at the cell membrane, trans-Golgi network, and endosomal compartments for multiple membrane traffic pathways, for example exo- and endocytosis. In addition, a subpopulation is used in SV formation at the PreAZ.

Interestingly, dendritic, axonal, or glial-derived spinules, representing a mechanism for extrasynaptic neuronal communication, and/or may function as structural "anchors" that increase the stability of cortical synapses were only very rarely observed in SBs in contrast to experimental animals where they were more frequently found (Rodriguez-Moreno et al. 2018, 2020).

Remarkably, beside synaptic complexes composed of a SBs with either a dendrite or a spine, also fine astrocytic processes identified by their darker appearance and the content of gliotransmitter (Fig. 3A framed area, see Supplemental Fig. 5) were frequently observed in L6a and L6b and were found close to dendritic profiles (Fig. 3A framed area, see Supplemental Fig. 5A) or provide astrocytic input to dendrites (see Supplemental Fig. 5B) or spines (see Supplemental Fig. 5C).

Overall, L6 SBs were on average medium-sized, with a mean surface area of 5.30 ± 1.21 μm^2, and a mean volume of 0.36 ± 0.12 μm^3, with only slight non-significant differences between L6a and L6b (Table 2; see Supplementary Table 2). The variability in surface area of SBs was relatively small in both L6a and L6b as indicated by a low CV and variance (Table 2) regardless of their target structures. L6 SBs were comparable in size with those in L5, but ~2-fold larger than those in L4 of the human TLN ($P \leq 0.001$; Table 2; see Supplementary Table 2). A strong correlation between the surface area and volume of SBs was observed for both sublaminae as indicated by the coefficient of correlation (R^2; Fig. 5A and *B*) that was significantly different between L6a and L6b ($P \leq 0.001$).

In most L6 SBs several mitochondria (range 1–5; Figs 3A–E,G and 4A–F,H) of different shape and size were observed, despite some SBs that only contained a single (Fig. 3G,H) or no mitochondrion (Figs 3F,4G,H) with a volume of 0.04 ± 0.02 μm^3 in L6a and 0.05 ± 0.04 μm^3 in L6b, respectively (Table 2).

Mitochondria contributed with ~7% (L6a) and ~6% (L6b) to the total bouton volume, with a ~2-fold lower percentage as that found for mitochondria in L5 (~12%, Table 2; see Supplementary Table 2) and L4 (~13%, Table 2; see Supplementary Table 2) of the human TLN.

A good correlation between the volume of the SBs and that of mitochondria (Fig. 5C,D) was found, suggesting, beside their function as energy suppliers, an important role of these structures as internal calcium stores and in the priming and docking process of SVs in the presynaptic bouton (for more details see Discussion; Südhof 2012).

Worth mentioning is the observation of a few degenerating SBs, characterized by their content of distorted organelles (not shown, but see Yakoubi et al. 2019a) and the occurrence of degenerating neurons (see Supplemental Fig. 4A) although sometimes still to be seen receiving synaptic input (see Supplemental Fig. 4B).

Structural Composition of AZs in L6a and L6b Excitatory SBs in the Human TLN

The number, size and shape of the AZs are important key structural determinants in synaptic transmission and plasticity (Matz et al. 2010; Holderith et al. 2012; reviewed by Cowan et al. 2002). The majority (~98%) of SBs in L6a and L6b had only a single (Figs 3A–D,F,G, 4, and 7) at most two AZs (Figs 3A,B1 and 4E; see also Table 2). Beside very large AZs (0.19 μm^2 in L6a and 0.27 μm^2 in L6b) spanning the entire pre- and postsynaptic apposition zone (Figs 3F,H and 4F), also smaller AZs (0.17 μm^2 in L6a, 0.12 μm^2 in L6b) covering only a fraction of the pre- and postsynaptic apposition zone were found (Figs 3A,D,G and 4C,G).

Table 2 Comparative quantitative analysis of various structural parameters in L4, L5, and L6 of the human TLN

	Layer	Mean ± SD	Median	IQR	CV	Skewness	Variance
		Synaptic boutons					
Surface area (μm^2)	L6	5.30 ± 1.21	5.23	1.77	0.23	−0.29	1.47
	L6a	5.12 ± 0.31	4.99	0.57	0.06	1.57	0.09
	L6b	5.48 ± 1.86	6.06	3.59	0.34	−1.26	3.47
	L5	6.09 ± 0.92	6.05	0.87	0.15	4.49#	23.04
	L4	2.50 ± 1.78	2.05	1.67	0.72	1.97	3.24
Volume (μm^3)	L6	0.63 ± 0.13	0.62	0.24	0.21	0.54	0.01
	L6a	0.53 ± 0.08	0.51	0.15	0.15	1.23	0.006
	L6b	0.72 ± 0.11	0.71	0.22	0.15	0.53	0.01
	L5	0.63 ± 0.18	0.63	0.21	0.29	2.05	0.46
	L4	0.16 ± 0.16	0.11	0.12	1.01	2.89	0.03
		Active zones					
PreAZ surface area (μm^2)	L6	0.19 ± 0.05	0.18	0.05	0.26	0.88	0.002
	L6a	0.18 ± 0.01	0.18	0.02	0.05	0.00	0.0001
	L6b	0.19 ± 0.06	0.18	0.15	0.32	0.59	0.006
	L5	0.23 ± 0.05	0.22	0.07	0.22	1.86	0.03
	L4	0.13 ± 0.07	0.11	0.08	0.54	1.35	0.005
PSD surface area (μm^2)	L6	0.18 ± 0.05	0.17	0.06	0.28	1.38	0.003
	L6a	0.17 ± 0.02	0.17	0.03	0.12	0.94	0.0002
	L6b	0.19 ± 0.08	0.17	0.16	0.42	1.03	0.007
	L5	0.29 ± 0.15	0.23	0.16	0.52	2.77	0.06
	L4	0.13 ± 0.07	0.11	0.08	0.53	1.44	0.005
Cleft width (nm)	L6	L: 19.75 ± 1.87	L: 19.85	L: 2.39	L: 0.09	L: −0.18	L: 3.48
		C: 22.94 ± 0.79	C: 22.90	C: 0.89	C: 0.03	C: 0.24	C: 0.62
	L6a	L: 18.76 ± 1.80	L: 19.85	L: 3.55	L: 0.10	L: −0.78	L: 3.23
		C: 22.54 ± 0.71	C: 22.96	C: 1.37	C: 0.03	C: −1.22	C: 0.62
	L6b	L: 20.73 ± 1.60	L: 20.73	L: 3.09	L: 0.08	L: 1.20	L: 2.55
		C: 23.33 ± 0.76	C: 23.33	C: 1.38	C: 0.03	C: 1.70	C: 0.58
	L5	L: 17.25 ± 2.39	L: 17.51	L: 3.74	L: 0.13	L: 1.14	L: 20.73
		C: 19.05 ± 2.94	C: 18.85	C: 2.95	C: 0.15	C: 1.82	C: 30.84
	L4	L: 14.11 ± 0.69	L: 14.43	L: 1.19	L: 0.05	L: 0.74	L: 8.86
		C: 16.47 ± 1.85	C: 15.72	C: 3.26	C: 0.11	C: 0.80	C: 17.09
		Mitochondria					
Volume (μm^3)	L6	0.05 ± 0.02	0.05	0.03	0.40	1.17	0.0005
	L6a	0.04 ± 0.02	0.04	0.01	0.15	1.73	0.00003
	L6b	0.05 ± 0.04	0.05	0.07	0.80	0.42	0.0012
	L5	0.12 ± 0.09	0.07	0.16	0.75	8.22#	50.30
	L4	0.03 ± 0.04	0.02	0.02	1.04	3.71#	0.001
% to the total volume	L6	6.70 ± 1.72	6.33	3.22	0.26	0.63	2.97
	L6a	6.89 ± 1.19	7.01	1.42	0.17	−0.44	1.41
	L6b	6.50 ± 2.43	5.15	4.25	0.37	1.73	5.88
	L5	12.04 ± 1.20	11.89	2.18	0.10	0.57	23.04
	L4	13.11 ± 6.20	12.78	9.25	0.47	0.17	38.47

Note: Summary of various structural parameter measurements provided from the detailed 3D-volume reconstructions of SBs in L6, separated for both sublaminae. For comparison, data for L5 (Yakoubi et al. 2019a) and L4 (Yakoubi et al. 2019b) of the human TLN are given. Values are given as mean SD, Median, IQR, CV, Skewness and Variance for each parameter in all patients investigated. #: Values with a skewness > 3 indicating non-normal distributions. *Abbreviations:* L: lateral; and C: central.

AZs were of the macular, non-perforated type (Figs 3A–D,F,G, 4A–H, and 6C,E,F) or showed either a perforation in the PreAZ or the PSD or both (Figs 3E,H and 6A,B,D).

On average, PreAZs were 0.18 ± 0.01 μm^2 in surface area in L6a and 0.19 ± 0.08 μm^2 in L6b, respectively (Table 2). The surface area of PSDs was 0.17 ± 0.02 μm^2 in L6a and 0.19 ± 0.08 μm^2 in

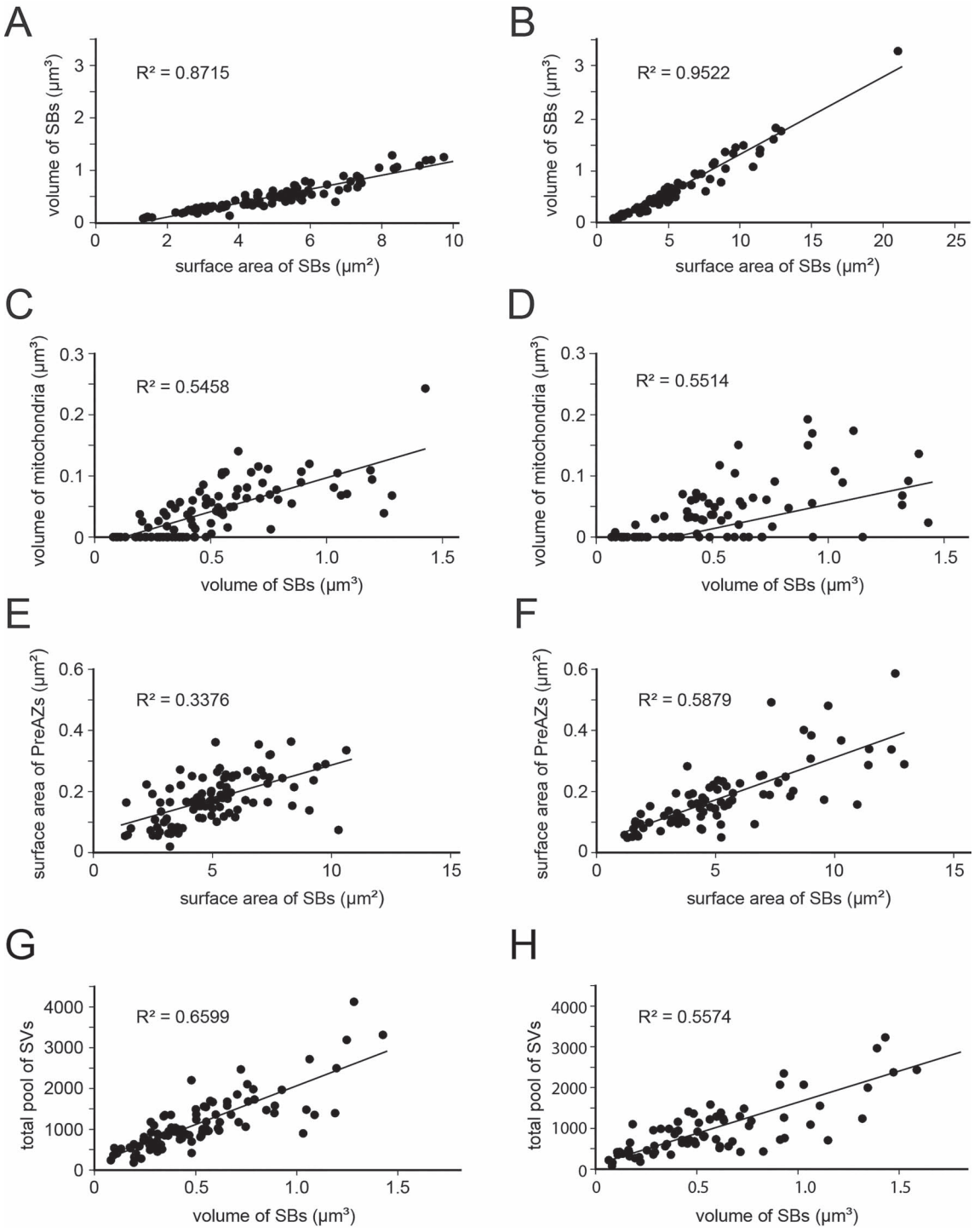

Figure 5. Correlations between various structural parameters of L6 SBs. Surface area of SBs versus volume of SBs in L6a (*A*) and L6b (*B*). Volume of SBs versus volume of mitochondria in L6a (*C*) and L6b (*D*). Surface area of SBs versus surface area of PreAZs in L6a (*E*) and L6b (*F*). Volume of SBs versus total pool of SVs in L6a (*G*) and L6b (*H*).

L6b. Both PreAZs and PSDs were significantly larger ($P \leq 0.001$) when compared with those in L4, but significantly smaller ($P \leq 0.001$) than those in L5 (Table 2; see Supplementary Table 2). However, L6 AZs did not show a large variability in both shape and size of the PreAZs and PSDs as those in L4 and L5 as indicated by the low SD, CV, and variance (Table 2) as described for other CNS synapses of similar or even larger size (see Discussion).

Remarkably, only a weak correlation between the mean surface area of SBs and that of PreAZs was found for L6a (Fig. 5E), but with a good and significantly different ($P \leq 0.001$) correlation for L6b (Fig. 5F). Finally, a good correlation also existed between

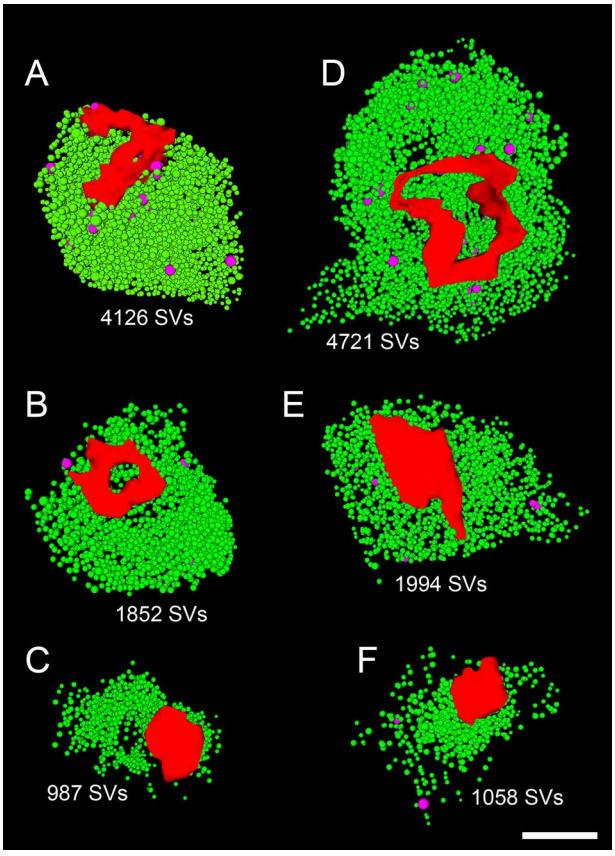

Figure 6. Pool of synaptic vesicles in L6 of the human TLN. (*A*, *D*) Representative examples of comparatively large vesicle pools in L6a (*A*) and L6b (*D*). (*B*, *E*) Two examples of medium-sized vesicle pools in L6a (*B*) and L6b (*E*). (*C*, *F*) Two examples of comparatively smaller vesicle pools in L6a (*C*) and L6b (*F*). In all 3D-reconstructions vesicles are given in green, DCVs in magenta and PreAZs in red. Note the differences in the shape and size of the PreAZs ranging from macular, non-perforated (*C*, *E*, *F*) to ring- (*B*, *D*) and horseshoe-like (*A*) forms. Scale bar 0.5 μm.

the volume of SBs and the total pool of SVs (Fig. 5G,H) suggesting that both the size of SBs and PreAZs contribute and partially determine the total pool of SVs. This is different to findings in L4 and L5 of the human TLN where the total pool size of SVs seemed to be independent from both structural parameters (Yakoubi et al. 2019a, 2019b).

The width of the synaptic cleft (Table 2; see Supplementary Table 2) at AZs in L6 ($n = 4$ patients, $n = 120$ AZs) was on average 19.75 ± 1.87 nm for the lateral, and 22.94 ± 0.79 nm for the central region with slight, but non-significant differences between the two sublaminae. The values are comparable with cleft width measured at L5 AZs, but significantly larger ($P \leq 0.05$) by 1.4-fold than that at AZs in L4 ($P \leq 0.01$) of the human TLN (Table 2; see Supplementary Table 2).

Organization of the Pools of SVs in L6a and L6b Excitatory SBs of the Human TLN

SVs are, beside the shape and size of AZs, another key structural element that contain, store, and release neurotransmitters, and hence play a fundamental role in synaptic transmission and in modulating short- and long-term synaptic plasticity (Südhof 2012, reviewed by Cowan et al. 2002). Their distribution in synaptic terminals and organization into three distinct functionally defined pools, namely the RRP, the RP, and the resting pool, regulate synaptic efficacy, strength and determine the mode and probability of release (uni- vs., multivesicular; uni- vs., multiquantal; Silver et al. 2003; Saviane and Silver 2006; Watanabe et al. 2013; Schikorski 2014; Vaden et al. 2019; reviewed by Schneggenburger et al. 2002; Rizzoli and Betz 2004, 2005; Neher 2015; Chamberland and Tóth 2016).

In general, SVs were distributed throughout the entire terminal in ~90% of the population of SBs investigated (Figs 3, 4, and 6). Interestingly, in some SBs the population of SVs was either densely packed throughout the terminal (Figs 4B–D and 6A–E) or near the PreAZs (Figs 4E–H and 6F).

Different types of vesicles were found (Table 3; see Supplementary Table 2): 1) small clear SVs with an average diameter of 33.32 ± 4.25 nm (L6a) and 32.19 ± 1.44 nm (L6b), 2) nearly 2-fold larger clear SVs, and 3) large DCVs with an average diameter of 62.99 ± 5.96 nm with no significant difference for the vesicles types between both sublaminae. DCVs were intermingled with the population of the SVs throughout the entire SB (Figs 4D,G,H and 6A,B,D–F). Their location with the SBs implies possible functions for DCVs, namely their role in endo- and exocytosis (Watanabe et al. 2013), build-up of PreAZs by releasing Piccolo and Bassoon (Schoch and Gundelfinger 2006), or by clustering SVs at the PreAZs (Mukherjee et al. 2010, Watanabe et al. 2013). In addition, various co-transmitters, such as neuropeptides, ATP, noradrenalin, and dynorphin were identified in large DCVs (Ghijsen and Leenders 2005; Zhang et al. 2011).

The average total pool of SVs was 1170.53 ± 318.17 (L6a) and 1059.17 ± 591.88 (L6b) SVs with an average of 1114.85 ± 429.35 for L6. Interestingly, the total pool size of SVs in L6a and L6b was significantly different ($P \leq 0.05$). SVs contributed with ~5% (0.03 μm^3) in L6a and ~4% (0.02 μm^3) in L6b to the total volume of SBs, however, with no significant difference between both sublaminae. Remarkably, a huge variability in total pool size exists in both sublaminae ranging from 178 to 4126 in L6a and 158 to 4721 in L6b, respectively (Table 3; see Supplementary Table 2).

Despite the slight but significant difference in the total pool size between L6a and L6b a good correlation between the volume of SBs and the total pool of SVs was observed (Fig. 5G,H). Interestingly, a lower correlation was found for the total pool of SVs and the surface area of PreAZs for both sublaminae, with a weak correlation for L6a (Fig. 7A) but a good correlation for L6b (Fig. 7B). The correlation factor for the total pool size with that of bouton volume and PreAZ surface area implies that the total pool of SVs is partially dependent from the size of the SBs and PreAZs.

The distribution pattern of SVs made it impossible to morphologically distinguish the three functionally defined pools of SVs, except for the "docked" and fused vesicles primed to the PreAZ (reviewed by Rizzoli and Betz 2004, 2005; Denker and Rizzoli 2010; Neher 2015; Chamberland and Tóth 2016; see also chapter on EM tomography).

To overcome this problem a perimeter analysis was performed to determine the exact location (distance) of each SV from the PreAZ. Thus, we assumed that the RRP was located at a distance (perimeter *p*) of ≤ 10 and ≤ 20 nm (less than the diameter of a SV in L6a and L6b) from the PreAZ representing "docked" and primed SVs fused to the PreAZ. The second pool, the RP, is constituted by SVs within 60–200 nm, which maintained release on moderate (physiological) stimulation. The resting pool,

Table 3 Comparative quantitative analysis of various SV parameters in L4, L5, and L6 of the human TLN

	Layer	Mean ± SD	Median	IQR	CV	Skewness	Variance
		Synaptic vesicles					
Total number of SVs	L6	1114.85 ± 429.35	1007.79	760.23	0.39	0.40	184,344.2
	L6a	1170.53 ± 318.17	1154.75	635.76	0.27	0.22	101,234.0
	L6b	1059.17 ± 591.88	860.83	1132.82	0.56	1.34	350,326.3
	L5	1518.52 ± 303.18	1347.21	541.98	0.19	2.39	165,5452.24
	L4	1820.64 ± 980.34	1544.5	1119.5	0.54	0.91	961,066.6
Volume (μm^3)	L6	0.03 ± 0.01	0.02	0.02	0.33	0.49	0.0002
	L6a	0.03 ± 0.01	0.02	0.02	0.43	1.73	0.00013
	L6b	0.02 ± 0.02	0.02	0.03	0.65	0.94	0.00023
	L5	0.05 ± 0.02	0.05	0.03	0.40	3.60#	0.002
	L4	0.01 ± 0.01	0.01	0.01	1.28	3.95#	0.0002
Diameter (nm)	L6	32.75 ± 2.90	32.65	4.42	0.09	0.04	8.43
	L6a	33.32 ± 4.25	34.39	8.29	0.13	−1.06	18.04
	L6b	32.19 ± 1.44	31.45	2.59	0.045	1.70	2.08
	L5	36.69 ± 1.71	37.02	3.26	0.04	−2.07	153.21
	L4	19.80 ± 5.63	18.00	0.28	3.41	2.10	31.69
		Pool size of SVs					
Putative RRP at p10 nm	L6	12.70 ± 4.32	13.53	8.19	0.34	−0.61	18.71
	L6a	9.91 ± 4.17	12.05	7.46	0.42	−1.70	17.35
	L6b	15.49 ± 4.48	15.00	8.92	0.29	0.49	20.07
	L5	5.42 ± 4.09	4.93	6.29	0.75	2.17	39.93
	L4	20.20 ± 18.58	17.00	27.25	0.92	1.11	345.04
Putative RRP at p20 nm	L6	28.70 ± 9.84	27.53	18.60	0.34	0.01	105.82
	L6a	23.41 ± 6.83	25.95	12.94	0.29	−1.44	46.70
	L6b	33.99 ± 12.84	29.10	24.25	0.38	1.46	164.95
	L5	15.21 ± 9.02	13.55	16.34	0.59	2.06	206.69
	L4	48.59 ± 39.02	41.00	53.00	0.80	1.17	1523.1
Putative RP 60–200 nm	L6	155.94 ± 35.10	146.29	35.35	0.23	2.15	1232.1
	L6a	148.68 ± 92.69	138.50	114.00	0.62	1.41	8590.9
	L6b	161.25 ± 102.57	143.00	119.50	0.64	1.93	10,521.1
	L5	181.86 ± 27.05	180.89	47.42	0.15	1.25	11,469.9
	L4	382.10 ± 248.23	313.00	376.79	0.65	1.41	61,617.5
Putative resting pool	L6	894.11 ± 412.49	813.62	806.87	0.46	0.67	17,8917.9
> 200 nm	L6a	966.34 ± 318.86	960.17	637.64	0.33	0.09	10,1674.8
	L6b	821.87 ± 506.12	667.07	976.09	0.62	1.25	25,6161.0
	L5	1264.07 ± 301.77	1150.76	540.39	0.24	0.66	72,853.5
	L4	1251.82 ± 471.17	541.00	471.17	0.38	1.70	87,678.3

Note: Summary of various synaptic parameter measurements provided from the detailed 3D-volume reconstructions of SBs in L6, and separated for both sublaminae. For comparison, data for L5 (Yakoubi et al. 2019a) and L4 (Yakoubi et al. 2019b) of the human TLN are given. Mean ± SD, Median, IQR, CV, Skewness and Variance are given for each parameter in all patients investigated. Values with a skewness > 3 indicate non-normal distributions. *Abbreviations:* p10, p20: perimeter from AZ (see Material and Methods).

consisted of all SVs further than ≥200 nm, preventing depletion upon strong or repetitive stimulations, but which under normal physiological conditions remains unused.

Using these criteria, the p10 nm RRP/AZ was relatively and comparatively large with an average of 9.91 ± 4.17 SVs (L6a) and 15.49 ± 4.48 SVs (L6b), respectively (Table 3; see Supplementary Table 2). The p10 nm RRP for L6b was significantly ($P \leq 0.001$) larger by ∼1.5-fold than that in L6a. For the p20 nm RRP/AZ the values increased by 2.4-fold (23.41 ± 6.83 in L6a) and by 2.2-fold (33.99 ± 12.84 in L6b) but were also significantly different by ∼1.5-fold between both sublaminae ($P \leq 0.001$). When compared with values taken from L5 and L4 of the human TLN, the p10 nm RRP in L6a was ∼2.3-fold larger than that in L5, but ∼0.6-fold smaller when compared with L4, respectively. The p10 nm RRP in L6b was ∼1.8-fold larger compared with L5 values, but ∼2-fold smaller than the p10 nm RRP in L4 (Table 3; see Supplementary Table 2).

For the p20 nm RRP values in L6a were nearly 1.5-fold larger than in L5, but ∼2-fold smaller when compared with values in L4. For L6b these values were 2.2-fold larger than in L5 but 1.5-fold smaller than in L4 (Table 3; see Supplementary Table 2). This strongly suggests layer-specific differences in the RRP in the human TLN.

Interestingly, both RRPs in L6a and L6b were characterized by a comparatively lower variability than in L5 and L4 as indicated by the SD, CV, and variance (Table 3; see Supplementary Table 2) also pointing to layer-specific differences in release probability, synaptic efficacy, strength and paired-pulse behavior at individual SBs. Strikingly, only a weak correlation, with the exception of the p20 nm RRP in L6b, was found for the p10 nm and p20 nm RRP with the surface area of PreAZs (Fig. 7C–F) in contrast to values obtained for CA1 synapses (Matz et al. 2010). Interestingly, the summation of the p10 nm and p20 nm RRP was only weakly correlated in L6a (Fig. 7G), but good correlated in L6b (Fig. 7H).

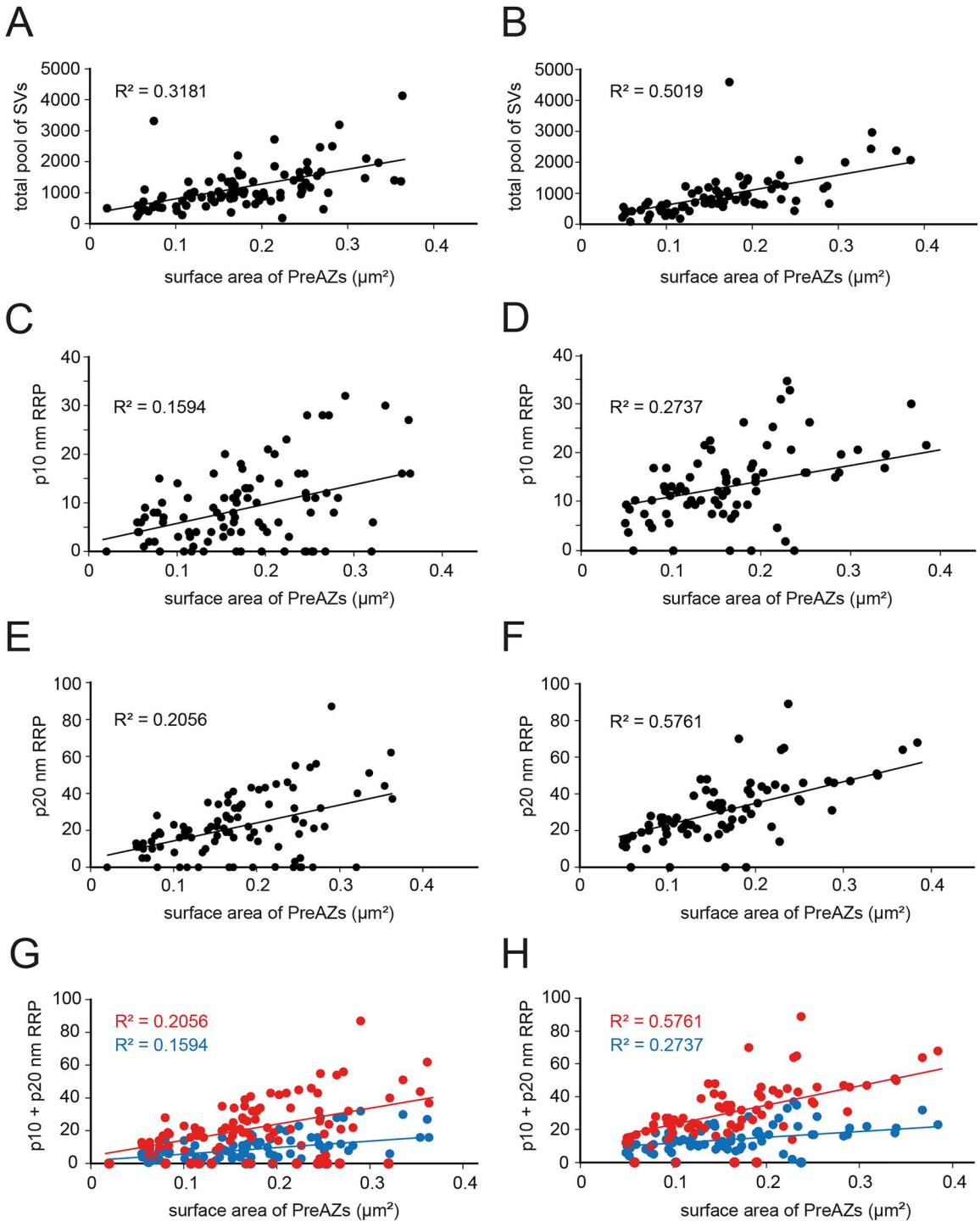

Figure 7. Correlations between various synaptic parameters of L6 SBs and SVs. Surface area of PreAZs versus total pool of SVs in L6a (*A*) and L6b (*B*). Surface area of PreAZs versus p10 nm RRP in L6a (*C*) and L6b (*D*). Surface area of PreAZs versus p20 nm RRP in L6a (*E*) and L6b (*F*). Surface area of PreAZs versus p10 + p20 nm RRP in L6a (*G*) and L6b (*H*).

The RP/AZ at 60–200 nm perimeter was 148.68 ± 92.69 SVs in L6a and 161.25 ± 102.57 in L6b with no significant difference for both sublaminae (Table 3; see Supplementary Table 2). For L6a, the RP was smaller compared with L5 and L4 by nearly 1.2-fold and 2.5-fold, respectively. For L6b the values were 1.1-fold and 2.4-fold smaller. No correlation for the RP (p60 nm) with the PreAZ was found for L6a (Fig. 8A), in contrast for L6b a good correlation was observed (Fig. 8B). For both sublaminae, a good correlation was also found using the p100 nm criterion (Fig. 8C,D).

The resting pool contained on average 966.34 ± 318.86 SVs in L6a and 821.87 ± 506.12 SVs in L6b, respectively, which was significantly different between both sublaminae ($P \leq 0.01$; Table 3; see Supplementary Table 2). The number of SVs in the resting

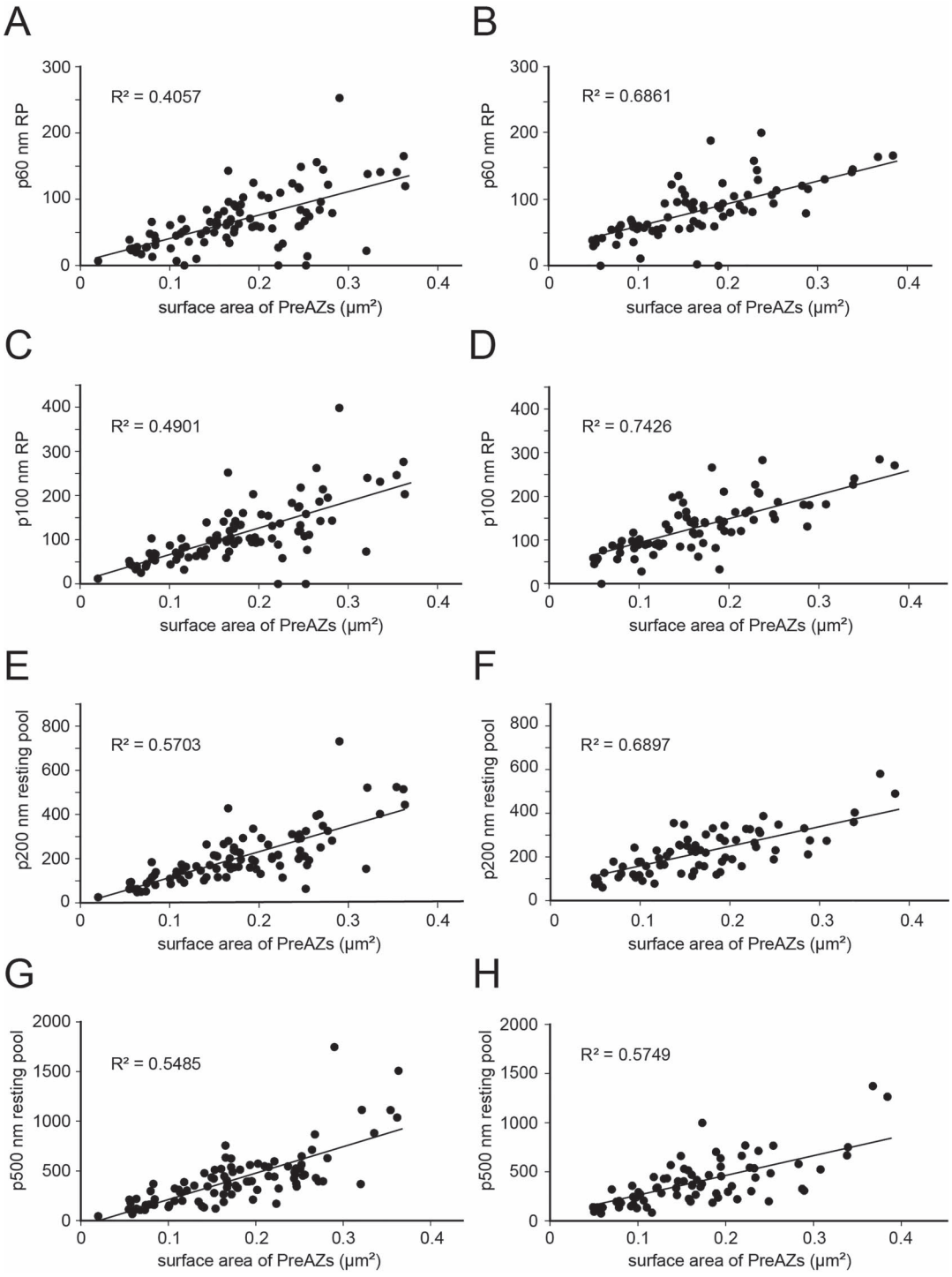

Figure 8. Correlations between various synaptic parameters of L6 SBs and SVs. Surface area of PreAZs versus p60 nm RP in L6a (*A*) and L6b (*B*). Surface area of PreAZs versus p100 nm RP in L6a (*C*) and L6b (*D*). Surface area of PreAZs versus p200 nm resting pool in L6a (*E*) and L6b (*F*). Surface area of PreAZs versus p500 nm resting pool in L6a (*G*) and L6b (*H*).

pool in L6a was 1.3-fold and 1.5-fold in L6b smaller when compared with the resting pools in L5 and L4. A good correlation existed for the resting pool (p200 nm, Fig. 8*E*,*F*) and the p500 nm perimeter criterion (Fig. 8*G*,*H*) with the surface area of the PreAZ similar to findings in L5 excitatory SBs in the human TLN (Yakoubi et al. 2019a).

Taken together, SBs in L6a and L6b are comparatively medium-sized in surface area and volume, with comparatively large overlapping PreAZs and PSDs and had either larger RRPs when compared with L5 SBs but smaller ones than SBs in L4 of the human TLN. The RP and resting pools in both L6a and L6b were smaller than in L5 and L4. In contrast to L5

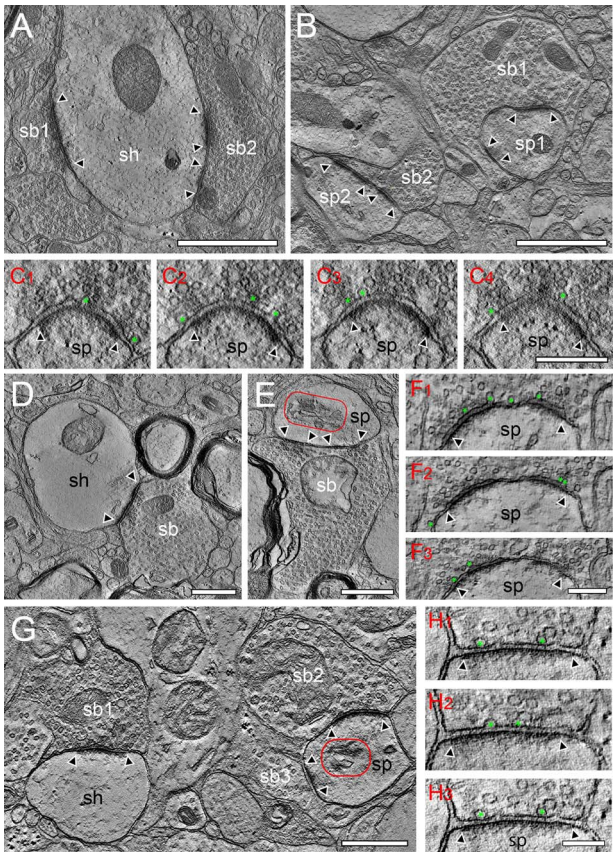

Figure 9. EM tomography of SBs in L4, L6a, and L6b in the human TLN. (*A*) Two SBs (sb1, sb 2) terminating on a large dendritic shaft (sh) in L4. Scale bar 1 μm. (*B*) Two spine synapses (sp1, sp2) with two separated AZs receiving synaptic input from two SBs (sb1, sb2) in L4. Scale bar 1 μm. (*C1–C4*) Sequence of images taken from a tilt-series of an individual PreAZ at a L4 spine (sp) synapse showing the location of "docked" SVs (green asterisks). Scale bar 0.25 μm. (*D*) Typical example of a shaft (sh) dendrite receiving synaptic input of a comparatively large SB (sb) in L6a. Scale bar 0.5 μm. (*E*) Dendritic spine in L6a (sp) identified by the presence of a prominent spine apparatus (framed area) receiving input from a relatively large, putative GABAergic SB (sb) as identified by the shape and size of the AZ and SVs. Scale bar 0.5 μm. (*F1–F3*) Sequence of three images taken from a tilt series of an individual PreAZ in an L6a SB terminating on a spine (sp) showing the location of "docked" SVs (green asterisks) at the PreAZ. Scale bar 0.25 μm. (*G*) Three SBs (sb–sb3) terminating on a small caliber dendritic shaft (sh, sb1) and on a dendritic spine (sp, sb2, and sb3) containing a spine apparatus (framed area) in L6b. Scale bar 0.25 μm. (*H1–H3*) Sequence of three images taken from a tilt series in an L6b SB terminating on a spine (sp) showing the location of "docked" SVs (green asterisks) at the PreAZ. Scale bar 0.25 μm. In all images the AZ is marked by arrowheads.

and L4, all pools showed a smaller variability and were better correlated.

EM Tomography of L4 Excitatory SBs in the Human TLN

High-resolution EM tomography was carried out on a total of 315 SBs out of three patients (Table 4). Only SBs where the AZ could be followed from its beginning to its end and where the AZ was cut perpendicular were included in our sample. In L6a 112 SBs (on spines = 63; on shafts = 43), in L6b 78 SBs (on spines = 38; on shaft = 39) and in L4 126 SBs (on spines = 75; on shafts = 51) were analyzed on a sample of small to large SBs and AZs to look for the organization of SVs at the PreAZ, in particular those of the RRP (Figs 9 and 10; see Supplementary Movie 1). In addition, this analysis was performed to test the hypothesis that larger PreAZs display more "docked" or fused (omega-shaped) SVs than smaller ones. As already mentioned above, SBs in L4 were also analyzed because both layers receive direct thalamic input and are also interconnected with each other (Marx and Feldmeyer 2013; Marx et al. 2017).

The results of the EM tomography were three-fold: First, only a minority (5%) of all PreAZs analyzed, regardless of their target structures, a dendritic shaft (Fig. 9*A*,*D*,*G*) or spine (Fig. 9*B*,*E*,*G*; see Supplementary Movie 1), contained none, but their majority (95%) more than one, the most 16 (L6a, L6b, Fig. 10) and 22 "docked" SVs at L4 spine AZs (Fig. 9C1–C4, *F1–F3*, *H1–H3*, 11; Table 4) and/or omega-shaped bodies (Fig. 9C3, C4, *F1*, *H2*; see Supplementary Movie 1), already fused (Fig. 9C1–C4, *F1–F3*, *H1–H3*; see Supplementary Movie 1) with the PreAZ. This strongly suggests multivesicular release of SVs at both, the L6 sublaminae and L4 SBs.

On average 3.43 ± 2.83 docked SVs (L6a), 6.29 ± 3.79 docked SVs (L6b), and 7.63 ± 4.29 docked SVs (L4) were found at individual PreAZs (Table 4). Strikingly, the number of "docked" SVs at L6b and L4 PreAZs was ~2-fold larger in L6b and L4 when compared with L6a, but ~3-fold (L6a), ~2.5-fold (L6b), and ~2.6-fold (L4) smaller to the results of our quantitative perimeter analysis for the p10 nm criterion (compare Tables 3 and 4). Secondly, all values of "docked" SVs, regardless which layer or sublamina, obtained by EM tomography were characterized by a relatively large variability as indicated by the SD, skewness and variance (Table 4). These findings were in line with that of the perimeter analysis. Third, there was a non-significant tendency that larger PreAZs contained more "docked" vesicles (Fig. 9C1–C4, *F1–F3*, *H1–H3*) providing a larger "docking" area allowing the recruitment of more SVs. However, in several cases also SBs with a smaller PreAZ were found that had the same number of "docked" vesicles (Fig. 9) when compared with larger SBs or AZs.

In addition, significant differences between L4 shaft and spine synapses with those in L6a and L6b and between L6a and L6b were found (Fig. 10).

CA of SBs in L6 of the Human TLN

There is growing interest in further classifying SBs upon structural criteria using different methods. Here, a CA became an attractive tool to determine further putative subtypes of excitatory SBs in a given layer based on their structural parameters. We adopted this method to meet the purpose above, based on standardized reproducible steps in already published articles about SBs in different layers and species (Yakoubi et al. 2019a, 2019b; Prume et al. 2020; Rodriguez-Moreno et al. 2020).

In this study, the CA was performed to further determine putative subtypes of excitatory SBs in L6a and L6b based on the structural parameters investigated of the human TLN (Figs 11, 12). The PCA showed two principal components (PCs; PC1 and PC2) explaining the most variance (Fig. 11); where PreAZs, PSDs and SV pools were the main features (parameters) that predominantly contributed to the PCs as visualized by the dendrograms for L6a (Fig. 11A) and L6b (Fig. 11C) and respective scatterplots (L6a Fig. 11B; L6b Fig. 11D). The PCA showed that the surface area of the PreAZs and PSDs as well as the vesicle pools, at different perimeters from the PreAZs, were the main structural parameters that equally contributed best to the PCs and best separated the SBs in L6a and L6b.

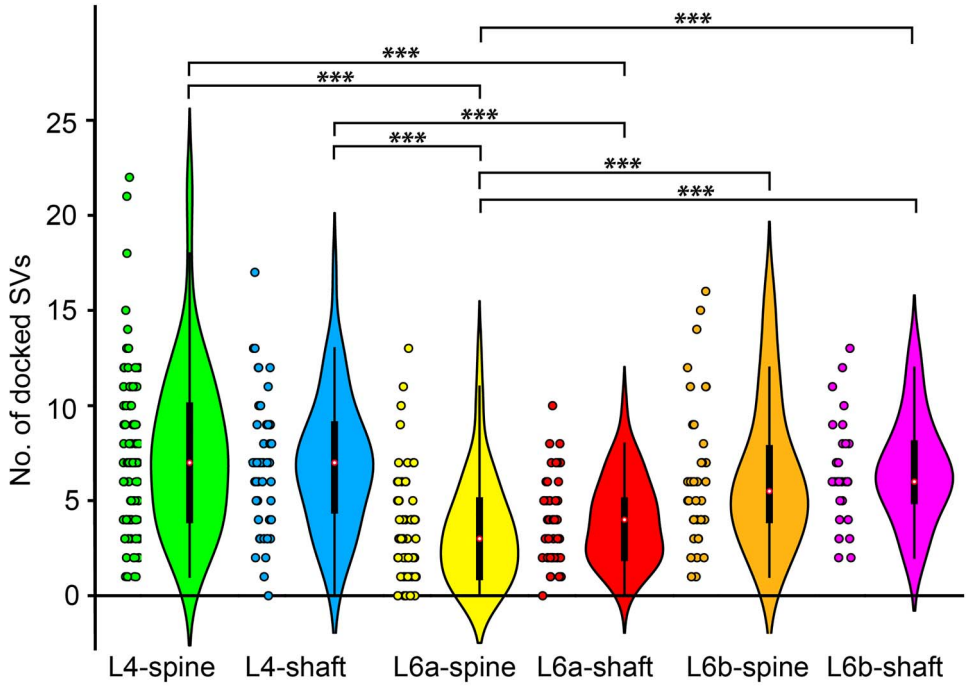

Figure 10. Violin and dot plots of the density and distribution of "docked" vesicles in the thalamocortical receiving layers L4 and L6 of the human TLN. Here, the distributions of "docked" SVs in L4, L6a, and L6b are given in different colors separated for spine and shaft SBs. The median in the violin plots is indicated by the red dot, IQRs (black areas), and minimum and maximum (vertical lines) for the distribution of "docked" SVs. Levels of significance are given by asterisks: $^{*}P \leq 0.05$; $^{**}P \leq 0.01$; and $^{***}P \leq 0.001$.

Table 4 "Docked" SVs in the thalamocortical afferent receiving layers in the human TLN

	Layer	Mean ± SD	Median	IQR	CV	Skewness	Variance
Number of "docked" vesicles	**L6** ($n = 179$ SVs)	4.71 ± 3.18	4.00	4.00	0.67	0.96	10.08
	L6a	3.69 ± 3.96	3.00	3.00	0.70	0.89	6.67
	Spine SBs ($n = 63$ SVs)	3.45 ± 2.83	3.00	4.00	0.82	1.17	7.93
	Shaft SBs ($n = 49$ SVs)	3.98 ± 2.22	4.00	3.50	0.55	0.47	4.98
	L6b	6.41 ± 3.35	6.00	4.00	0.52	0.83	11.25
	Spine SBs ($n = 38$ SVs)	6.29 ± 3.79	5.50	4.25	0.60	0.97	14.37
	Shaft SBs ($n = 29$ SVs)	6.59 ± 2.73	5.00	3.00	0.41	0.48	7.47
	L4	7.32 ± 3.96	7.32	5.25	0.54	0.91	15.71
	Spine SBs ($n = 75$ SVs)	7.63 ± 4.29	7.00	6.00	0.56	0.99	18.37
	Shaft SBs ($n = 51$ SVs)	6.86 ± 3.42	7.00	5.00	0.50	0.47	11.72

Note: Values are given as mean ± SD, Median, IQR, CV, Skewness and Variance.

Hence, dendrograms (Fig. 12A,C,E,G) and scatter plots (Fig. 12B,D,F,H) were generated from the HCA for each sublamina to identify and better visualize the different SB clusters. Note that only clusters were considered that remain stable after shuffling and sorting of the dataset in a different order. The dissimilarity between the clusters is indicated by the Euclidean height in the dendrograms (Fig. 12A,C,E,G).

Thus, the clustering according to the PreAZ and PSD surface area led to two major groups of SBs (Fig. 12A,B). In L6a: First, the green cluster with 0.26 ± 0.05 μm^2 (PreAZ) and 0.25 ± 0.05 μm^2 (PSD); which is 2-fold larger in size than the second blue cluster with 0.13 ± 0.05 μm^2 and 0.12 ± 0.04 μm^2 for PreAZ and PSD surface areas, respectively. In L6b (Fig. 12C,D), three groups were obtained: the green cluster with 0.22 ± 0.06 μm^2 (PreAZ) and 0.21 ± 0.07 μm^2 (PSD), also 2-fold larger than the blue cluster that had 0.12 ± 0.05 μm^2 (PreAZ) and 0.11 ± 0.05 μm^2 (PSD). The third cluster in red was larger in size (as it contained few SBs) with 0.53 ± 0.18 μm^2 (PreAZ) and 0.53 ± 0.15 μm^2 (PSD).

Based on the SV pools at p10–p20 nm, p30–p400 nm, and p500 nm from the PreAZs, two major groups of excitatory SBs were revealed in L6a (Fig. 12E,F), where one cluster is almost 2-fold larger than the other one, whereas, three distinct groups of SBs were found in L6b (Fig. 12G,H). The sizes of these clusters are summarized in Table 5 for better visualization and comparison.

In summary, based on the clustering algorithms used, the strongest structural parameters that best characterized excitatory SBs in L6a and L6b of the human TLN were first, the PreAZ and PSD surface area that revealed two major groups of SBs in both L6a and L6b, and second, the vesicle pool size at different perimeters from the PreAZs, revealing two groups of SBs in L6a and three in L6b.

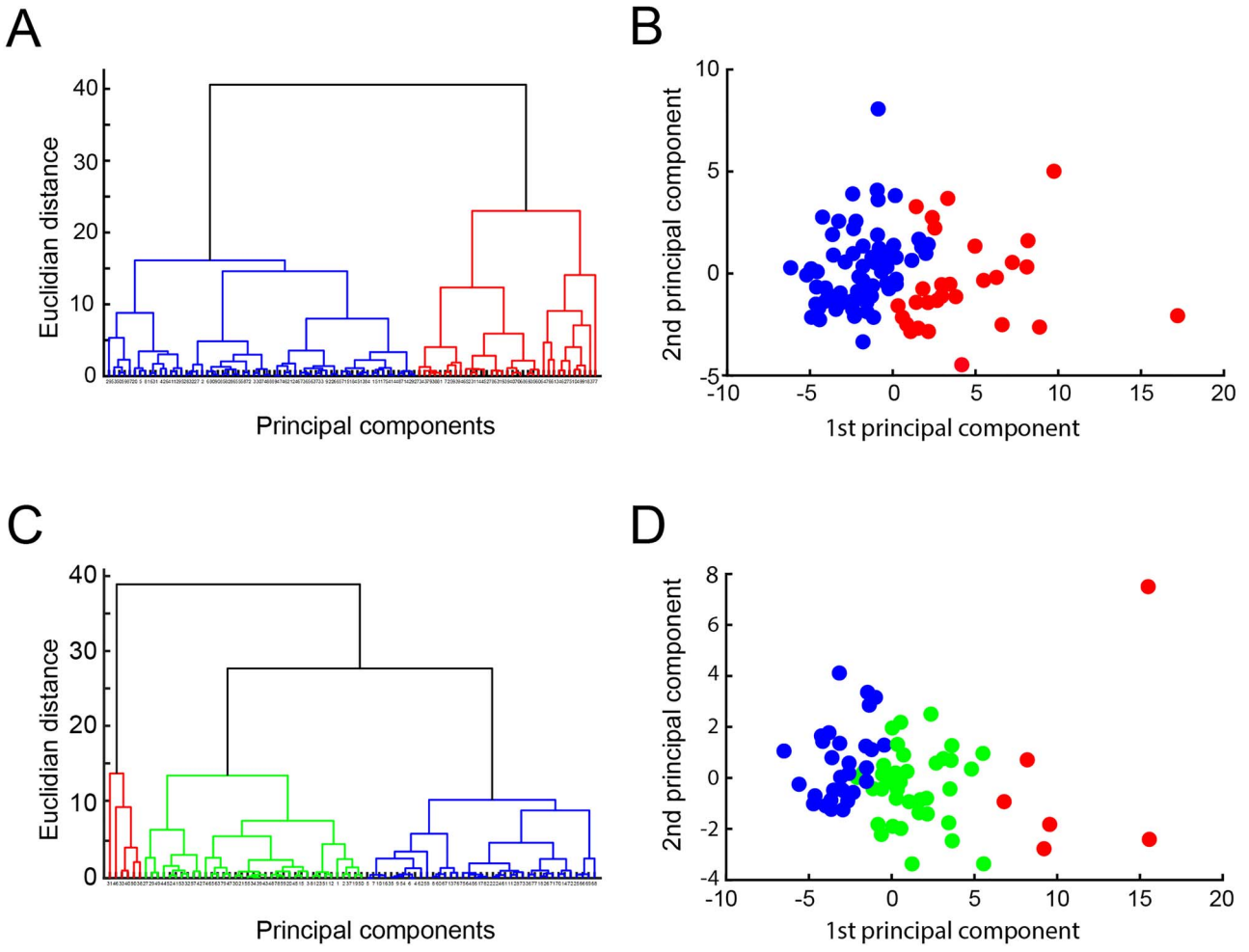

Figure 11. CA of structural parameters in L6a and L6b in the human TLN. (*A*, *C*) Dendrograms of the CA performed for all structural parameters investigated separated for L6a (*A*) and L6b (*C*). (*B*, *D*) Scatterplots of the CA performed for all structural parameters investigated separated for L6a (*B*) and L6b (*D*). Note the difference in clustering between the two sublaminae.

Astrocytic Coverage of L6 SBs in the Human TLN

Astrocytes, by directly interacting with synaptic complexes, play an important role in the induction, maintenance and termination of synaptic transmission and plasticity (Min and Nevian 2012; Krencik et al. 2017; reviewed by Dallérac et al. 2018). In L6a and L6b of the human TLN, astrocytes and their fine processes were observed in both sublaminae of the human TLN intermingled with neurons and synaptic complexes, composed of the SBs and dendritic shafts or spines (Fig. 13A,B). Strikingly, and in contrast to L4 and L5 of the human TLN where the volume fraction of astrocytic processes was ~60% (L5) and ~80% (L4), only ~20% of synaptic complexes were completely covered in L6. As a consequence, a high number of synaptic complexes was only partially covered or completely unsheathed by astrocytic processes (Fig. 13A,C), whereas only a small fraction of synaptic complexes was tightly ensheathed by astrocytic processes (Fig. 13B,C).

This finding strongly suggests a layer-specific coverage of synaptic complexes by astrocytes and their fine processes. Hence, it is most likely that the absence of fine astrocytic processes at the majority of human L6 synaptic complexes together with the abundance of myelinated and clusters of unmyelinated axons may partially contribute to a different "behavior" in the induction, maintenance and termination of synaptic transmission and plasticity. In particular, the removal of "spilled" horizontally diffusing neurotransmitter molecules that may prevent inter-synaptic crosstalk by fine astrocytic processes. In addition, both structural subelements also represent a physical barrier for neurotransmitter diffusion (Fig. 13B; see also Discussion).

Discussion

The present study is the first comprehensive, coherent structural and quantitative study of the synaptic organization of L6 in the human TLN using fine-scale TEM, 3D-reconstructions and EM tomography.

Overall, no significant differences were found between structural and synaptic parameters between L6a and L6b SBs, despite significant differences in the RRP of SVs as shown by the perimeter and EM tomography analysis.

Thus, the dual origin of both sublaminae from the ventricular zone and cortical plate (L6a) and the primordial zone or cortical

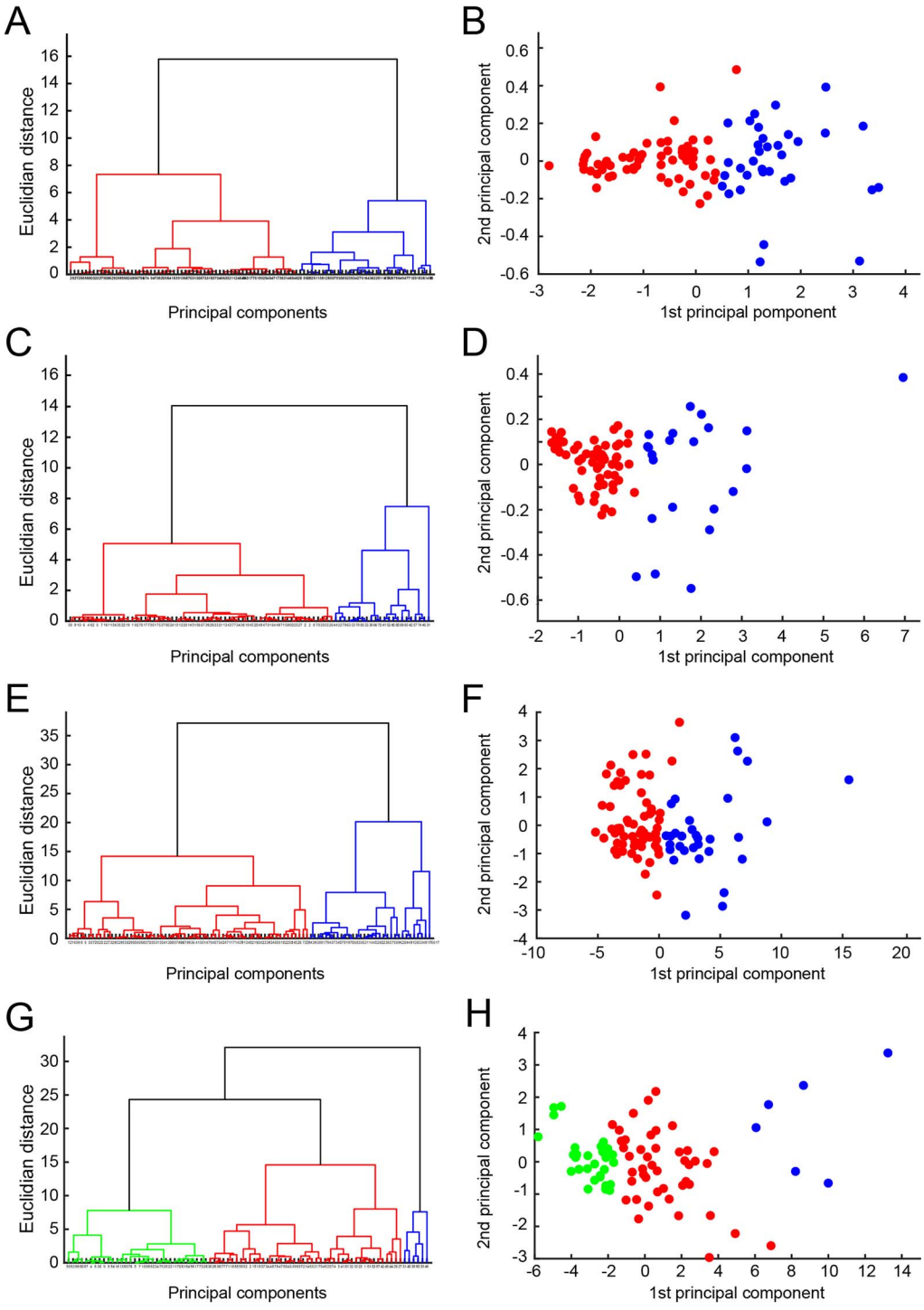

Figure 12. CA of PreAZs, PSDs and vesicle pools in L6a and L6b in the human TLN. (*A*, *C*) Dendrograms of the CA performed for the PreAZs and PSDs separated for L6a (*A*) and L6b (*C*). (*B*, *D*) Scatterplots of the CA performed for the PreAZs and PSDs separated for L6a (*B*) and L6b (*D*). (*E*, *G*) Dendrograms of the CA performed for the pools of SVs separated for L6a (*E*) and L6b (*G*). (*F*, *H*) Scatterplots of the CA performed for the pools of SVs separated for L6a (*F*) and L6b (*H*). Note the difference in clustering between the two sublaminae.

subplate (L6b) seems not to be reflected in the structural composition and quantitative morphology of SBs in both sublaminae. The total pool size and the comparatively large RRP and RP suggest that L6 SBs are strong, efficient, and reliable in synaptic transmission. On the other hand, the large variability in the shape and size of AZs and that of the three pools of SVs at individual L6 SBs also point to a strong modulation of short-term plasticity in L6 itself (Voigts et al. 2020) but also in the network of the human TLN (see also Varga et al. 2015; Molnár et al. 2016; Seeman et al. 2018).

Table 5 Size of SV pools at different perimeters from the PreAZ in L6a and L6b of the human TLN

SV pools at different distances (nm) from the PreAZ	L6a		L6b		
	First cluster (green)	Second cluster (blue)	First cluster (green)	Second cluster (blue)	Third cluster (red)
p10–p20 nm	16.43 ± 12.82	10.95 ± 7.47	22.78 ± 7.11	9.30 ± 4.86	49.17 ± 10.94
p30–p400 nm	470.86 ± 264.73	239.37 ± 128.76	382.14 ± 139.38	197.25 ± 91.13	1019. 67 ± 331.85
p500 nm	604.31 ± 341.85	305.85 ± 159.16	502.30 ± 179.79	242.70 ± 101.96	1386.50 ± 384.64

Note: Values are given as mean ± SD.

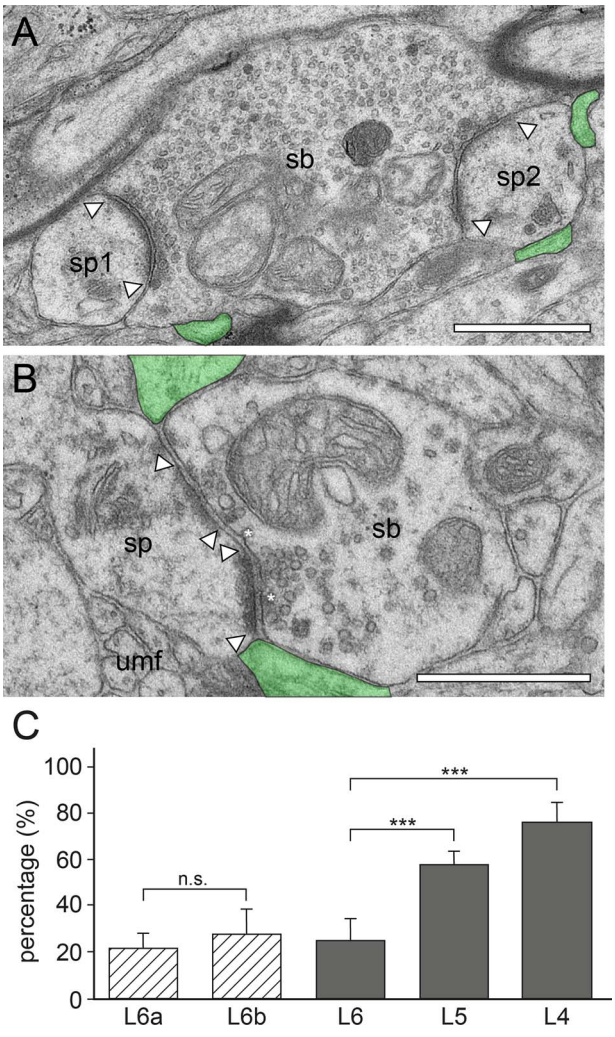

Figure 13. Astrocytic coverage of synaptic complexes in L6 of the human TLN. (A) Electron micrograph of a large synaptic bouton (sb) terminating on two opposite spines (sp1, sp2) in L6a. AZs are marked by arrowheads. Note the large distance and thus absence of fine astrocytic processes (transparent green) at the AZs of the synaptic complexes. Scale 0.5 μm. (B) Higher magnification of a synaptic complex between an SB (sb) and a dendritic spine (sp) containing a spine apparatus in L6b. Here, astrocytic processes (transparent green) were found close to the AZ. Sometimes, synaptic complexes were accompanied by clusters of unmyelinated fibers (umf). Note two "docked" SVs (white asterisks) at the PreAZ. The two AZs are also marked by arrowheads. Scale 0.5 μm. (C) Bar histograms showing the percentage (mean ± SD) of the volumetric fraction of astrocytic processes. Note that no significant differences are found between L6a and L6b. For comparison, values estimated for L5 and L4 are also given that are significantly different (***$P \leq 0.001$) from that obtained in L6 (mean of pooled data of L6a and L6b).

Since SBs in L6, like those in L4 receive direct thalamic input and both layers are strongly interconnected with each other, L6 SBs may act as "amplifiers," "integrators" but also as "discriminators" for columnar specific, long-range extracortical, and cortico-thalamic signals from the sensory periphery.

Shape and Size of AZs in L6: Major Determinants of Synaptic Transmission and Plasticity?

Although SBs are composed of nearly the same structural subelements, it is their individual and thus highly specific structural composition that makes them unique entities, perfectly adapted to their function in a given network, microcircuit, or brain region.

Meanwhile it is unquestionable that structural parameters of SBs, in particular the shape and size of AZs represent one structural key element that determines synaptic efficacy, strength, modes of release, and probability of release, but are also involved in the modulation of short- and long-term synaptic plasticity (Matz et al. 2010; Südhof 2012; Holderith et al. 2012; Wilhelm et al. 2014; Vaden et al. 2019). The majority of L6 SBs in the human TLN had only a single AZ, like those in human L4 and L5 SBs and other cortical SBs of similar size in rodents and NHPs (Marrone et al. 2005; Nava et al. 2014; Rollenhagen et al. 2015, 2018; Bopp et al. 2017; Hsu et al. 2017). Strikingly, the surface area of AZs in L6 and L5 SBs in the human TLN was on average ~0.2 μm^2 (Yakoubi et al. 2019a) and thus on average 1.1-fold larger when compared with AZ size of L4 and L5 SBs in rats (Rollenhagen et al. 2015, 2018). However, they were ~2- to 3-fold larger than those in mouse and NHP visual, motor, and somatosensory neocortex (Bopp et al. 2017; Hsu et al. 2017), despite AZs in L4 of the human TLN that were comparable in size (Yakoubi et al. 2019b). Remarkably, AZs in L6 and L5 of the human TLN are even larger than those at the Calyx of Held (Spirou et al. 1998; Sätzler et al. 2002; Wimmer et al. 2006), the cerebellar (Xu-Friedman et al. 2003), and hippocampal mossy fiber boutons (Rollenhagen et al. 2007), which are much larger in surface area by ~500-, ~14–55-, and ~6–50-fold.

The large variability in AZ size at individual SBs in both experimental animals and the human TLN may partially contribute to differences in the mode of release (uni- or multivesicular; uni- or multiquantal), quantal size, the size of the RRP and release probability as shown for other CNS synapses (Matz et al. 2010; Freche et al. 2011; Holderith et al. 2012; Vaden et al. 2019; reviewed by Neher 2015; Chamberland and Tòth 2016).

It is worth mentioning that a large proportion (~85%) of AZs in L6 SBs is established on spines of different shape. The majority of them (92% in L6a and 90% in L6b) contained a spine apparatus, an endoplasmic organelle involved in increasing spine motility. Spine "apparati" not only guarantee spine motility, but also were shown to partially contribute in modulating short- and long-term potentiation by stabilizing the

axo-spinous complex during initial and high-frequency stimulation (Holtmaat et al. 2005; Umeda et al. 2005). Moreover, on spines ~65% of the AZs occupied two-third or even the entire pre- and postsynaptic apposition zone, suggesting that excitatory synaptic transmission is highly efficient by increasing the docking area for primed and "docked" SVs. This is further supported by our EM tomography experiments (see Fig. 9) where larger AZs tend to have more "docked" SVs than smaller ones.

Interestingly, only a weak (L6a) and in contrast a good (L6b) correlation between the PreAZ surface area with that of the bouton was found with differences to rat and human cortical L4 and L5 excitatory SBs (Rollenhagen et al. 2015, 2018; Yakoubi et al. 2019a, 2019b). This may imply that the size of the AZs is an independent structural parameter and may be regulated in an activity-dependent manner as shown for hippocampal SBs in the CA1 subregion (Matz et al. 2010; Holderith et al. 2012).

In addition, both L6 sublaminae differed in their correlation of the surface area of PreAZs and the total pool of SVs, with a weak correlation for L6a and a good correlation for L6b that is also different from those in neocortical L4 and L5 in rat (Rollenhagen et al. 2015, 2018) and in the human TLN (Yakoubi et al. 2019a, 2019b).

In summary, the comparatively large size, perfect overlap and relatively high number of perforated PreAZs and PSDs at L6 SBs in the human TLN may partially contribute to a high release probability, and thus reliable synaptic transmission (Marx and Feldmeyer 2013; Marx et al. 2017; Seeman et al. 2018; Voigts et al. 2020). On the other hand, the large variability in AZ size at individual SBs in both sublaminae of L6 may play a role in the modulation of synaptic plasticity and paired-pulse behavior at individual SBs (Seeman et al. 2018) and during Up-and-Down states of synaptic activity in the neocortex (Voigts et al. 2020).

Size of the Three Pools of SVs

The second major key structural parameter is the availability of SVs and their recycling rates during prolonged and high-frequency synaptic activity. Hence, the size of the RRP, RP, and even the resting pool critically determines synaptic efficacy, strength, mode of release, and plasticity (Rizzoli and Betz 2004; Schikorski 2014; Watanabe et al. 2013 Rollenhagen et al. 2015; Vaden et al. 2019; reviewed by Rizzoli and Betz 2005; Neher 2015; Chamberland and Tóth 2016).

L6 SBs in the human TLN had a total pool size of ~1200 SVs/AZ in L6a and ~1100 SVs/AZ in L6a; significantly smaller than that observed in L4 and L5 terminals in the human TLN, but 2-fold and ~1.5-fold larger than their counterparts in cortical L4 and L5 in rats, respectively (Rollenhagen et al. 2015, 2018). The total pool/AZ was even larger by ~1.5-fold and nearly 9-fold when compared with even much larger CNS terminals such as the hippocampal (Rollenhagen et al. 2007) and cerebellar Mossy Fiber Boutons (Xu-Friedmann and Regehr 2003) and the Calyx of Held endterminal (Sätzler et al. 2002).

The putative RRP was on average 9.91 ± 4.17 (p10 nm) and doubled to 23.41 ± 6.83 (p20 nm) SVs/AZ in L6a and 15.49 ± 4.48 (p10 nm) and 33.99 ± 12.84 (p20 nm) in L6b, larger by ~1.5- to 3-fold than in L5 SBs, but smaller by ~1.5-fold and comparable with those in L4 of the human TLN, but comparatively larger by 3–8-fold than in L4 and L5 SBs in rats, respectively. Comparison with even larger CNS synaptic terminals the difference in the RRP was even more pronounced and revealed a more than 12-fold (hippocampal MFBs p10 nm 1.6 ± 1.5, p20 nm 6.2 ± 4.1; Rollenhagen et al. 2007) and 8-fold (Calyx of Held p10 nm 1.9 ± 2.0, p20 nm 4.8 ± 3.8; Sätzler et al. 2002) difference.

Interestingly, our estimates of the size of the RRP using the perimeter analysis is by ~3-fold (L6a) and nearly 2.5-fold (L6b) larger for the p10 criterion than our measurements using EM tomography. However, this difference can be explained by the inclusion of SVs that are not "docked" but within 10-nm distance from the PreAZ, whereas only "docked" SVs were counted using EM tomography.

In conclusion, the number of SVs in the RRP strongly indicates multivesicular release and also suggests a high availability of SVs in the RRP to even high-frequency synaptic stimulation.

This statement is also supported by the size of the putative RP/AZ, which was ~150 SVs at human L6a and L6b SBs, comparable with that in L5 SBs in both rat and human neocortex, but ~2.5-fold smaller than in L4 of the human TLN. Again, although much smaller in bouton size, the RP/AZ in L6 of the human TLN was nearly 3-fold larger than that reported for the rat Calyx of Held (~60 vesicles).

Finally, the resting pool of SVs (on average ~900 SVs) in L6 SBs is large enough to rapidly replenish the RRP and RP and may thus guarantee only a partial depletion even at repetitive high-frequency stimulation by rapid refilling via active transfer with the help of mitochondria associated with the pool of SVs (Verstreken et al. 2005; Smith et al. 2016).

Taken together, the comparatively large size of AZs together with the size of three pools of SVs in L6 of the human TLN provide the basis for high reliability, but also modulation in synaptic transmission, efficacy and strength (Seeman et al. 2018; Voigts et al. 2020). However, the marked differences in AZ and SV pool sizes between individual SBs, even between L6a and L6b, may underlie rapid changes in the computational properties, modulation of synaptic plasticity and during Up-and-Down states in behavior (Zhou and Fuster 1996, Sanchez-Vives and McCormick 2000; Sakata and Harris 2009; Testa-Silva et al. 2014; Voigts et al. 2020).

Other Important Structural Subelements that Contribute to Synaptic Transmission and Plasticity

Two other structural parameters may be of importance and may thus also partially contribute to synaptic transmission and plasticity, namely mitochondria in the presynaptic bouton, and the astrocytic ensheathment of SBs.

Mitochondria are structural components present in all CNS nerve terminals but with marked difference in their numbers. Remarkably, mitochondria in L6 SBs contribute only to ~7% to the total volume, a value nearly 2-fold smaller than in L4 and L5 SBs of the human TLN (Yakoubi et al. 2019a, 2019b), but were also closely associated with the pool of SVs pointing also to a role of mitochondria in the transfer of SVs from the resting pool to the RP and RRP in L6a and L6b as shown for L4 and L5 of the human TLN (Smith et al. 2016; Yakoubi et al. 2019a, 2019b). In addition, mitochondria are highly mobile, act as internal calcium stores and hence regulate internal Ca^{2+} levels in nerve terminals (Perkins et al. 2010; Papouin et al. 2017; reviewed by Allen 2014; Dallérac et al. 2018).

Taken together mitochondria in L6, although lower in number, may contributed to the induction and maintenance of several signal cascades, for example the binding, priming and docking process of SVs, relying on the rapid availability of Ca^{2+} in the SB.

Secondly, and the most striking difference between L6, L4, and L5 of the human TLN was the coverage of synaptic complexes by fine astrocytic processes (Fig. 13). Astrocytic processes reaching as near as the synaptic cleft can control and regulate the spatial and temporal glutamate concentration in the synaptic cleft (reviewed by Allen 2014; Dallérac et al. 2018). In contrast to L4 and L5 with an astrocytic volume fraction of ~80% (L4) and ~65% (L5)a leading to a nearly complete astrocytic coverage of synaptic complexes, those in L6 had only an astrocytic volume fraction of ~20% showing as a consequence either no or only a partial coverage of synaptic complexes with astrocytic processes. This percentage is even much lower than that at CA1 synapses where ~50% of fine astrocytic processes were found at the synaptic interface (Ventura and Harris 1999). Our finding of the astrocytic coverage in L6 suggests that astrocytic processes do not uniformly sample and remove glutamate at the synaptic cleft. Hence, it is most likely that glutamate spillover may occur at the majority of L6 synaptic complexes not ensheathed by astrocytic complexes. This allows also a horizontal diffusion of glutamate in the synaptic cleft not controlled by the uptake by glutamate transporters located at fine astrocytic processes. This may, as a consequence, support synaptic cross talk between adjacent synaptic complexes and thus a switch from asynchronous to synchronous release of adjacent synaptic complexes upon repetitive stimulation (von Gersdorff and Borst 2002; Hallermann et al. 2003).

Thus, astrocytes at L6 synaptic complexes can only partially act as physical barriers to neurotransmitter diffusion and may allow a longer duration of the glutamate concentration in the synaptic cleft at a comparatively high number of synaptic complexes. As a consequence, astrocytes are only partially involved in the termination of synaptic transmission and hinder a speed-up recovery from receptor desensitization (Oliet et al. 2004; Haydon and Carmignoto 2006; reviewed by Dallérac et al. 2018).

In summary, two other structural subelements at L6 excitatory SBs in human TLN contribute to synaptic transmission and plasticity but also show marked laminar-specific difference in the human TLN and also to findings in experimental animals (see above).

L6: A Unique Layer in the Cortical Column with Specialized Functions

In general, L6 is present in all neocortical areas across mammalian species, but is unique with respect to its dual origin and the impact and balance of thalamo- versus intracortical input. In the somatosensory and visual cortices of rodents, cats and monkeys, L6 beside L4 is regarded as the main recipient layer for thalamo-cortical afferents originating from the specific relay nuclei (but see Constantinople and Bruno 2013; Rodriguez–Moreno et al. 2018, 2020; reviewed by Sherman 2012; Clascá et al. 2016). In these species, L6a is composed of two distinct populations of pyramidal neurons, cortico-thalamic (CT) and cortico-cortical (CC) projection neurons (Zhang and Deschênnes 1997, 1998; Kumar and Ohana 2008; Marx and Feldmeyer 2013; Qi and Feldmeyer 2016; Marx et al. 2017). The CT projecting pyramidal neurons can be further subdivided with respect to their intracortical projection pattern and axonal termination zone. The first population of CT pyramidal neurons possesses a predominantly intracolumnar axonal projection with axonal collaterals in L4 that terminate at the L4/L3 border. Possible target neurons are other pyramidal neurons in L6, L5, spiny stellate, and star pyramidal neurons in L4 (Lee and Sherman 2008, Marx and Feldmeyer 2013; Marx et al. 2017) and to a smaller fraction inhibitory neurons in those layers (Frandolig et al. 2019).

The second population of CT neurons in L6a projects predominantly to and innervate L5a and other L6a pyramidal neurons with columnar axonal collaterals but also long-range horizontal collaterals that also could span several columns. In rodents, a small third subpopulation of CT pyramidal neurons with a more local axonal projection in L6a and few collaterals in L5b was described (Zhang and Deschênnes 1997, 1998).

In contrast, CC projection pyramidal neurons of L6a intermingled with the CT projecting pyramidal neurons are characterized by a dense axonal plexus in L6a and L5b with a few collaterals in L6b. These collaterals either remain within the cortical "home" column in which the somata of these neurons are located but also project and interconnect neighboring columns via long-range horizontal axonal collaterals, with terminations in different cortical regions, such as motor and sensory areas and a transcallosal projection to the other hemisphere (Zhang and Deschênnes 1997, 1998) although these collaterals are restricted to L6.

In summary, CT and CC projection pyramidal neurons in L6a are involved in both intracortical columnar and transcolumnar signal processing. TC projection neurons control their thalamocortical input originating from the specific thalamic relay nuclei due to a positive excitatory feed-back loop and thus control inputs from the sensory periphery. Hence, L6a may be involved in the integration, coordination and balancing of signals from other cortical but also extracortical brain regions.

In contrast to L6a, still relatively little is known about the synaptic organization of L6b. Due to its more diverse neuronal organization it has been speculated that L6b may represent a distinct layer (layer 7) constituted by persisting "subplate" neurons (Reep 2000). It is still rather unknown whether L6b also contains two subpopulations of pyramidal neurons although a small population of CT projecting neuron exists (Arimatsu and Ishida 2002). Golgi, intra- and extracellular injections studies revealed local intralaminar axonal collaterals and projections to the white matter, but also a transcolumnar long-range horizontal projection to the primary and secondary somatosensory and primary motor cortex (Tomböl et al. 1975; Tomböl 1984; Clancy and Cauller 1999; Arimatsu and Ishida 2002; Marx and Feldmeyer 2013).

One general function of the neocortex is to generate dynamic predictive models that include "expectations" of incoming stimuli and subsequent contextual appropriate actions. The ability to generate and update these models from the sensory environment enables rapid and adaptive changes in behavior that underlie cognitive functions such as flexible language processing, one important function of the human TLN. Such computation is found in visual (Courchesne et al. 1975), auditory (Ulanosky et al. 2003) and language-processing (Kutas and Hillyard 1980a, 1980b) areas. Electrophysiologically such change detection occur as an increase in firing rates elicited by deviant stimuli following stimulus-specific adaptation (Voigts et al. 2020).

In this context both sublaminae in L6 are well positioned to contribute to the neocortical implementation of predictive models, as it integrates and balance thalamic, columnar, long-range cortico-cortical, and modulatory inputs from other sensory areas such as somatosensory and motor cortex (Zhang and Deschênes 1998; Zhang et al. 2014; Vélez-Fort et al. 2014; reviewed by Thomson 2010). It has been shown by a recent study that stronger L6 drive inhibited firing and suppressed

overall sensory function. These findings indicate that, despite their sparse activity, specific ensembles of stimulus-driven L6 neurons are required to form neocortical predictions, and to realize their behavioral benefit (Voigts et al. 2020).

With respect to the synaptic organization of the human TLN these, together with our findings suggest, which due to a comparatively high density of synaptic complexes suggesting a high intracortical columnar connectivity, the predominant location of AZs on dendritic spines containing a spine apparatus, the shape and size of AZs and the comparatively large RRP and RP predict a high reliability, precision but also modulation of stimulus dependent sensory responses from and to various brain region with which the human TLN is interconnected.

Supplementary Material

Supplementary material is available at *Cerebral Cortex* online.

Notes

We would like to thank our technicians Ulrike Holz, Brigitte Marshallsay, and Tayfun Palaz for their equal excellent technical assistance and constant support. Some of this work was performed by use of the Deutsche Forschungsgemeinschaft funded maschinery ("INST 58219/40-1 FUGG" and "INST 58219/41-1 FUGG") at the Imaging Center Essen a service core facility of the Faculty of Medicine of the University Duisburg-Essen, Germany. We would also like to thank the Helmholtz Association of German Research Centers for their constant financial support (J.L.).

References

Allen NJ. 2014. Astrocyte regulation of synaptic behavior. *Annu Rev Cell Dev Biol*. 30:439–463.

Allone C, Lo Buono V, Corallo F, Pisani LR, Pollicino P, Bramanti P, Marino S. 2017. Neuroimaging and cognitive functions in temporal lobe epilepsy: a review of the literature. *J Neurol Sci*. 381:7–15.

Andjelic S, Gallopin T, Cauli B, Hill EL, Roux L, Badr S, Hu E, Tamas G, Lambolez B. 2009. Glutamatergic nonpyramidal neurons from neocortical layer VI and their comparison with pyramidal and spiny stellate neurons. *J Neurophysiol*. 101:641–654.

Anton-Sanchez L, Bielza C, Merchán-Peréz A, Rodriguez JR, DeFelipe J, Larranaga P. 2014. Three-dimensional distribution of cortical synapses: a replicated point pattern-based analysis. *Front Neuroanat*. 8:85. 10.3389/fnana.2014.00085.

Arimatsu Y, Ishida M. 2002. Distinct neuronal populations specified to form corticocortical and corticothalamic projections from layer VI of developing cerebral cortex. *Neuroscience*. 114:1033–1045.

Bopp R, Holler-Rickauer S, Martin KA, Schuhknecht GF. 2017. An ultrastructural study of the thalamic input to layer 4 of primary motor and primary somatosensory cortex in the mouse. *J Neurosci*. 37:2435–2448.

Boyer C, Schikorski T, Stevens CF. 1998. Comparison of hippocampal dendritic spines in culture and in brain. *J Neurosci*. 18:5294–5300.

Briggs F. 2010. Organizing principles of cortical layer 6. *Front Neural Circuits*. 4:3.

Chamberland S, Tóth K. 2016. Functionally heterogeneous synaptic vesicle pools support diverse synaptic signalling. *J Physiol*. 594:825–835.

Chen CC, Abrams S, Pinhas A, Brumberg JC. 2009. Morphological heterogeneity of layer VI neurons in mouse barrel cortex. *J Comp Neurol*. 512:726–746.

Clancy B, Cauller LJ. 1999. Widespread connections from the subgriseal neurons (layer VII) to layer 1 in the adult rat cortex. *J Comp Neurol*. 407:275–286.

Clascá F, Porrero C, Galazo MJ, Rubio-Garrido P, Evangelio M. 2016. Anatomy and development of multispecific thalamocortical axons: implications for cortical dynamic and evolution. In: Rockland KS, editor. *Axons brain archit*. Oxford: Academic Press, pp. 69–92.

Constantinople CM, Bruno RM. 2013. Deep cortical layers are activated directly by thalamus. *Science*. 340:1591–1594.

Courchesne E, Hillyard SA, Galambos R. 1975. Stimulus novelty, task relevance and the visual evoked potential in man. *Electroencephalogr Clin Neurophysiol*. 39:131–143.

Cowan M, Südhof TC, Stevens CF. 2002. *Synapses*. 1st ed. Baltimore, USA: Johns Hopkins University Press, pp. 1–656.

Dallérac G, Zapata J, Rouach N. 2018. Versatile control of synaptic circuits by astrocytes: where, when and how? *Nat Rev Neurosci*. 19:729–743.

DeFelipe J, Marco P, Busturia I, Merchán-Peréz A. 1999. Estimation of the number of synapses in the cerebral cortex: methodological considerations. *Cereb Cortex*. 9:722–732.

Denker A, Rizzoli SO. 2010. Synaptic vesicle pools: an update. *Front Synaptic Neurosci*. 2:135.

Diao Y, Cui L, Chen Y, Burbridge TJ, Han W, Wirth B, Sestan N, Crair MC, Zhang J. 2018. Reciprocal connections between cortex and thalamus contribute to retinal axonal targeting to dorsal lateral geniculate nucleus. *Cereb Cortex*. 28:1168–1182.

Dominguez-Alvaro M, Montero-Crespo M, Blazquez-Llorca L, DeFelipe J, Alonso-Nanclares L. 2019. 3D electron microscopy study of synaptic Organization of the Normal Human Transentorhinal Cortex and its possible alterations in Alzheimer's disease. *eNeuro*. 6:1–17.

Feldmeyer D. 2012. Excitatory neuronal connectivity in the barrel cortex. *Front Neuroanat*. 6:24.

Feldmeyer D, Lübke J. 2010. The axons of excitatory neurons in the neocortex. In: *New aspects of axonal structure and function*. New York Dordrecht Heidelberg London: Springer, pp. 157–178.

Fiala JC, Harris KM. 2001. Extending unbiased stereology of brain ultrastructure to three-dimensional volumes. *J Am Med Inform Assoc*. 8:1–16.

Frandolig JE, Matney CJ, Lee K, Kim J, Chevee M, Kim SJ, Bickert AA, Brown SP. 2019. The synaptic organization of layer 6 circuits reveals inhibition as a major output of a neocortical sublamina. *Cell Rep*. 28:3131–3143 e3135.

Freche D, Pannasch U, Rouach N, Holcman D. 2011. Synapse geometry and receptor dynamics modulate synaptic strength. *PLoS One*. 6:e25122.

Gray EG. 1959. Electron microscopy of synaptic contacts on dendrite spines of the cerebral cortex. *Nature*. 183:1592–1593.

Ghijsen WE, Leenders AG. 2005. Differential signaling in presynaptic neurotransmitter release. *Cell Mol Life Sci*. 62:937–954.

Hallermann S, Pawlu C, Jonas P, Heckmann M. 2003. A large pool of releasable vesicles in a cortical glutamatergic synapse. *Proc Natl Acad Sci U S A*. 100:8975–8980.

Hammer Ø, Harper AT, Ryan PD. 2001. Past: paleontological statistics software package for education and data analysis. *Palaeontologia Electronica*. 4:1–9.

Hay E, Segev I. 2015. Dendritic excitability and gain control in recurrent cortical microcircuits. *Cereb Cortex*. 25:3561–3571.

Haydon PG, Carmignoto G. 2006. Astrocyte control of synaptic transmission and neurovascular coupling. *Physiol Rev*. 86:1009–1031.

Holderith N, Lorincz A, Katona G, Rozsa B, Kulik A, Watanabe M, Nusser Z. 2012. Release probability of hippocampal glutamatergic terminals scales with the size of the active zone. *Nat Neurosci*. 15:988–997.

Holtmaat AJ, Trachtenberg JT, Wilbrecht L, Shepherd GM, Zhang X, Knott GW, Svoboda K. 2005. Transient and persistent dendritic spines in the neocortex in vivo. *Neuron*. 45:279–291.

Hsu A, Luebke JI, Medalla M. 2017. Comparative ultrastructural features of excitatory synapses in the visual and frontal cortices of the adult mouse and monkey. *J Comp Neurol*. 525:2175–2191.

Insausti R. 2013. Comparative neuroanatomical parcellation of the human and nonhuman primate temporal pole. *J Comp Neurol*. 521:4163–4176.

Kiernan JA. 2012. Anatomy of the temporal lobe. *Epilepsy Res Treat*. 2012:1–12. 10.1155/2012/176157.

Knott G, Holtmaat A. 2008. Dendritic spine plasticity–current understanding from in vivo studies. *Brain Res Rev*. 58:282–289.

Korogod N, Petersen CC, Knott GW. 2015. Ultrastructural analysis of adult mouse neocortex comparing aldehyde perfusion with cryo fixation. *Elife*. 4. 10.7554/eLife.05793.

Kremer JR, Mastronarde DN, McIntosh JR. 1996. Computer visualization of three-dimensional image data using IMOD. *J Struct Biol*. 116:71–76.

Krencik R, van Asperen JV, Ullian EM. 2017. Human astrocytes are distinct contributors to the complexity of synaptic function. *Brain Res Bull*. 129:66–73.

Kumar P, Ohana O. 2008. Inter- and intralaminar subcircuits of excitatory and inhibitory neurons in layer 6a of the rat barrel cortex. *J Neurophysiol*. 100:1909–1922.

Kutas M, Hillyard SA. 1980a. Reading between the lines: event-related brain potentials during natural sentence processing. *Brain Lang*. 11:354–373.

Kutas M, Hillyard SA. 1980b. Event-related brain potentials to semantically inappropriate and surprisingly large words. *Biol Psychol*. 11:99–116.

Lee CC, Sherman SM. 2008. Synaptic properties of thalamic and intracortical inputs to layer 4 of the first- and higher-order cortical areas in the auditory and somatosensory systems. *J Neurophysiol*. 100:317–326.

Mansvelder HD, Verhoog MB, Goriounova NA. 2019. Synaptic plasticity in human cortical circuits: cellular mechanisms of learning and memory in the human brain? *Curr Opin Neurobiol*. 54:186–193.

Marrone DF, LeBoutillier JC, Petit TL. 2005. Modeling behavioral recovery following lesion induction in the rat dentate gyrus. *Neurobiol Learn Mem*. 83:196–205.

Marx M, Feldmeyer D. 2013. Morphology and physiology of excitatory neurons in layer 6b of the somatosensory rat barrel cortex. *Cereb Cortex*. 23:2803–2817.

Marx M, Qi G, Hanganu-Opatz IL, Kilb W, Luhmann HJ, Feldmeyer D. 2017. Neocortical layer 6B as a remnant of the subplate - a morphological comparison. *Cereb Cortex*. 27:1011–1026.

Mastronarde DN. 2005. Automated electron microscope tomography using robust prediction of specimen movements. *J Struct Biol*. 152:36–51.

Matz J, Gilyan A, Kolar A, McCarvill T, Krueger SR. 2010. Rapid structural alterations of the active zone lead to sustained changes in neurotransmitter release. *Proc Natl Acad Sci U S A*. 107:8836–8841.

Mayhew TM. 1996. How to count synapses unbiasedly and efficiently at the ultrastructural level: proposal for a standard sampling and counting protocol. *J Neurocytol*. 25: 793–804.

Mercer A, West DC, Morris OT, Kirchhecker S, Kerkhoff JE, Thomson AM. 2005. Excitatory connections made by presynaptic cortico-cortical pyramidal cells in layer 6 of the neocortex. *Cereb Cortex*. 15:1485–1496.

Miller MW. 1988. Maturation of rat visual cortex: IV. The generation, migration, morphogenesis, and connectivity of atypically oriented pyramidal neurons. *J Comp Neurol*. 274:387–405.

Min R, Nevian T. 2012. Astrocyte signaling controls spike timing-dependent depression at neocortical synapses. *Nat Neurosci*. 15:746–753.

Mohan H, Verhoog MB, Doreswamy KK, Eyal G, Aardse R, Lodder BN, Goriounova NA, Asamoah B, Groot C, van der Sluis S, et al. 2015. Dendritic and axonal architecture of individual pyramidal neurons across layers of adult human neocortex. *Cereb Cortex*. 25:4839–4853.

Molnár G, Rozsa M, Baka J, Holderith N, Barzo P, Nusser Z, Tamas G. 2016. Human pyramidal to interneuron synapses are mediated by multi-vesicular release and multiple docked vesicles. *Elife*. 5:1–12. 10.7554/eLife.18167.

Mukherjee K, Yang X, Gerber SH, Kwon HB, Ho A, Castillo PE, Liu X, Südhof TC. 2010. Piccolo and bassoon maintain synaptic vesicle clustering without directly participating in vesicle exocytosis. *Proc Natl Acad Sci U S A*. 107:6504–6509.

Nava N, Chen F, Wegener G, Popoli M, Nyengaard JR. 2014. A new efficient method for synaptic vesicle quantification reveals differences between medial prefrontal cortex perforated and nonperforated synapses. *J Comp Neurol*. 522:284–297.

Neher E. 2015. Merits and limitations of vesicle pool models in view of heterogeneous populations of synaptic vesicles. *Neuron*. 87:1131–1142.

Oliet SH, Piet R, Poulain DA, Theodosis DT. 2004. Glial modulation of synaptic transmission: insights from the supraoptic nucleus of the hypothalamus. *Glia*. 47:258–267.

Papouin T, Dunphy J, Tolman M, Foley JC, Haydon PG. 2017. Astrocytic control of synaptic function. *Philos Trans R Soc Lond B Biol Sci*. 5:372.

Perkins GA, Tjong J, Brown JM, Poquiz PH, Scott RT, Kolson DR, Ellisman MH, Spirou GA. 2010. The micro-architecture of mitochondria at active zones: electron tomography reveals novel anchoring scaffolds and cristae structured for high-rate metabolism. *J Neurosci*. 30:1015–1026.

Prume M, Rollenhagen A, Yakoubi R, Sätzler K, Lübke JHR. 2020. Quantitative three-dimensional reconstructions of excitatory synaptic Boutons in the "barrel field" of the adult "Reeler" mouse somatosensory neocortex: a comparative fine-scale electron microscopic analysis with the wild type mouse. *Cereb Cortex*. 30:3209–3227.

Qi G, Feldmeyer D. 2016. Dendritic target region-specific formation of synapses between excitatory layer 4 neurons and layer 6 pyramidal cells. *Cereb Cortex*. 26:1569–1579.

Reep RL. 2000. Cortical layer VII and persistent subplate cells in mammalian brains. *Brain Behav Evol*. 56:212–234.

Rizzoli SO, Betz WJ. 2004. The structural organization of the readily releasable pool of synaptic vesicles. *Science*. 303:2037–2039.

Rizzoli SO, Betz WJ. 2005. Synaptic vesicle pools. *Nat Rev Neurosci*. 6:57–69.

Rodriguez-Moreno J, Rollenhagen A, Arlandis J, Santuy A, Merchán-Peréz A, DeFelipe J, Lübke JHR, Clascà F. 2018. Quantitative 3D ultrastructure of thalamocortical synapses from

the "Lemniscal" ventral posteromedial nucleus in mouse barrel cortex. *Cereb Cortex*. 28:3159–3175.

Rodriguez-Moreno J, Porrero C, Rollenhagen A, Rubio-Teves M, Casas-Torremocha D, Alonso-Nanclares L, Yakoubi R, Santuy A, Merchan-Perez A, DeFelipe J, et al. 2020. Area-specific synapse structure in branched posterior nucleus axons reveals a new level of complexity in thalamocortical networks. *J Neurosci*. 40:2663–2679.

Rollenhagen A, Sätzler K, Rodriguez EP, Jonas P, Frotscher M, Lübke JHR. 2007. Structural determinants of transmission at large hippocampal mossy fiber synapses. *J Neurosci*. 27:10434–10444.

Rollenhagen A, Klook K, Sätzler K, Qi G, Anstötz M, Feldmeyer D, Lübke JHR. 2015. Structural determinants underlying the high efficacy of synaptic transmission and plasticity at synaptic boutons in layer 4 of the adult rat 'barrel cortex'. *Brain Struct Funct*. 220:3185–3209.

Rollenhagen A, Ohana O, Sätzler K, Hilgetag CC, Kuhl D, Lübke JHR. 2018. Structural properties of synaptic transmission and temporal dynamics at excitatory layer 5B synapses in the adult rat somatosensory cortex. *Front Synaptic Neurosci*. 10:24. 10.3389/fnsyn.2018.00024.

Rowell JJ, Mallik AK, Dugas-Ford J, Ragsdale CW. 2010. Molecular analysis of neocortical layer structure in the ferret. *J Comp Neurol*. 518:3272–3289.

Sätzler K, Söhl LF, Bollmann JH, Borst JG, Frotscher M, Sakmann B, Lübke JHR. 2002. Three-dimensional reconstruction of a calyx of held and its postsynaptic principal neuron in the medial nucleus of the trapezoid body. *J Neurosci*. 22:10567–10579.

Sakata S, Harris KD. 2009. Laminar structure of spontaneous and sensory-evoked population activity in auditory cortex. *Neuron*. 64:404–418.

Sanchez-Vives MV, McCormick DA. 2000. Cellular and network mechanisms of rhythmic recurrent activity in neocortex. *Nat Neurosci*. 3:1027–1034.

Saviane C, Silver RA. 2006. Fast vesicle reloading and a large pool sustain high bandwidth transmission at a central synapse. *Nature*. 439:983–987.

Schikorski T. 2014. Readily releasable vesicles recycle at the active zone of hippocampal synapses. *Proc Natl Acad Sci U S A*. 111:5415–5420.

Schindelin J, Arganda-Carreras I, Frise E, Kaynig V, Longair M, Pietzsch T, Preibisch S, Rueden C, Saalfeld S, Schmid B, et al. 2012. Fiji: an open-source platform for biological-image analysis. *Nat Methods*. 9:676–682.

Schneggenburger R, Sakaba T, Neher E. 2002. Vesicle pools and short-term synaptic depression: lessons from a large synapse. *Trends Neurosci*. 25:206–212.

Schoch S, Gundelfinger ED. 2006. Molecular organization of the presynaptic active zone. *Cell Tissue Res*. 326:379–391.

Seeman SC, Campagnola L, Davoudian PA, Hoggarth A, Hage TA, Bosma-Moody A, Baker CA, Lee JH, Mihalas S, Teeter C, et al. 2018. Sparse recurrent excitatory connectivity in the microcircuit of the adult mouse and human cortex. *Elife*. 7:1–27. 10.7554/eLife.37349.

Sherman SM. 2012. Thalamocortical interactions. *Curr Opin Neurobiol*. 22:575–579.

Silver RA, Lübke J, Sakmann B, Feldmeyer D. 2003. High-probability uniquantal transmission at excitatory synapses in barrel cortex. *Science*. 302:1981–1984. 10.1126/science.1087160.

Smith HL, Bourne JN, Cao G, Chirillo MA, Ostroff LE, Watson DJ, Harris KM. 2016. Mitochondrial support of persistent presynaptic vesicle mobilization with age-dependent synaptic growth after LTP. *Elife*. 5:1–30. 10.7554/eLife.15275.

Spirou GA, Rowland KC, Berrebi AS. 1998. Ultrastructure of neurons and large synaptic terminals in the lateral nucleus of the trapezoid body of the cat. *J Comp Neurol*. 398:257–272.

Südhof TC. 2012. The presynaptic active zone. *Neuron*. 75:11–25.

Tai XY, Bernhardt B, Thom M, Thompson P, Baxendale S, Koepp M, Bernasconi N. 2018. Review: neurodegenerative processes in temporal lobe epilepsy with hippocampal sclerosis: clinical, pathological and neuroimaging evidence. *Neuropathol Appl Neurobiol*. 44:70–90.

Tamada H, Blanc J, Korogod N, Petersen CC, Knott GW. 2020. Ultrastructural comparison of dendritic spine morphology preserved with cryo and chemical fixation. *Elife*. 9:e56384.

Testa-Silva G, Verhoog MB, Linaro D, de Kock CP, Baayen JC, Meredith RM, De Zeeuw CI, Giugliano M, Mansvelder HD. 2014. High bandwidth synaptic communication and frequency tracking in human neocortex. *PLoS Biol*. 12:e1002007.

Thomson AM. 2010. Neocortical layer 6, a review. *Front Neuroanat*. 4:13.

Tömböl T, Hajdu F, Somogyi G. 1975. Identification of the Golgi picture of the layer VI cortico-geniculate projection neurons. *Exp Brain Res*. 24:107–110.

Tömböl T. 1984. Layer VI cells. In: Peters A, Jones EG, editors. *Cerebral Cortex*. Vol 1. London (NY): Plenum Press, pp. 479–510.

Ulanosly N, Las L, Nelken I. 2003. Processing of low-probability sounds by cortical neurons. *Nat Neurosci*. 6:391–398.

Umeda T, Ebihara T, Okabe S. 2005. Simultaneous observation of stably associated presynaptic varicosities and postsynaptic spines: morphological alterations of CA3-CA1 synapses in hippocampal slice cultures. *Mol Cell Neurosci*. 28:264–274.

Vaden JH, Banumurthy G, Gusarevich ES, Overstreet-Wadiche L, Wadiche JI. 2019. The readily-releasable pool dynamically regulates multivesicular release. *Elife* 31 pii: e47434. doi: 10.7554/eLife.47434.

Varga C, Tamas G, Barzo P, Olah S, Somogyi P. 2015. Molecular and electrophysiological characterization of GABAergic interneurons expressing the transcription factor COUP-TFII in the adult human temporal cortex. *Cereb Cortex*. 25:4430–4449.

Vélez-Fort M, Rousseau CV, Niedworok CJ, Wickersham IR, Rancz EA, Brown APY, Strom M, Margrie TW. 2014. The stimulus selectivity and connectivity of layer six principal cells reveals cortical microcircuits underlying visual processing. *Neuron*. 83:1431–1443.

Ventura R, Harris KM. 1999. Three-dimensional relationships between hippocampal synapses and astrocytes. *J Neurosci*. 19:6897–6906.

Verstreken P, Ly CV, Venken KJ, Koh TW, Zhou Y, Bellen HJ. 2005. Synaptic mitochondria are critical for mobilization of reserve pool vesicles at drosophila neuromuscular junctions. *Neuron*. 47:365–378.

Vogt BA. 2009. *Cingulate neurobiology and disease*. Oxford; New York: Oxford University Press.

Voigts J, Deister CA, Moore CI. 2020. Layer 6 ensembles can selectively regulate the behavioral impact and layer-specific representation of sensory deviants. *Elife*. 9:1–30.

von Economo C, Koskinas GN. 1925. *Die Cytoarchitektonik der Hirnrinde des erwachsenen Menschen*. Wien und Berlin, J. Springer.

von Gersdorff H, Borst JG. 2002. Short-term plasticity at the calyx of held. *Nat Rev Neurosci*. 3:53–56.

Watakabe A, Ichinohe N, Ohsawa S, Hashikawa T, Komatsu Y, Rockland KS, Yamamori T. 2007. Comparative analysis of layer-specific genes in mammalian neocortex. *Cereb Cortex*. 17:1918–1933.

Watanabe S, Rost BR, Camacho-Perez M, Davis MW, Sohl-Kielczynski B, Rosenmund C, Jorgensen EM. 2013. Ultrafast endocytosis at mouse hippocampal synapses. *Nature*. 504:242–247.

Wilhelm BG, Mandad S, Truckenbrodt S, Krohnert K, Schafer C, Rammner B, Koo SJ, Classen GA, Krauss M, Haucke V, et al. 2014. Composition of isolated synaptic boutons reveals the amounts of vesicle trafficking proteins. *Science*. 344:1023–1028.

Wimmer VC, Horstmann H, Groh A, Kuner T. 2006. Donut-like topology of synaptic vesicles with a central cluster of mitochondria wrapped into membrane protrusions: a novel structure-function module of the adult calyx of held. *J Neurosci*. 26:109–116.

Xu-Friedman MA, Regehr WG. 2003. Ultrastructural contributions to desensitization at cerebellar mossy fiber to granule cell synapses. *J Neurosci*. 23:2182–2192.

Yakoubi R, Rollenhagen A, von Lehe M, Shao Y, Sätzler K, Lübke JHR. 2019a. Quantitative three-dimensional reconstructions of excitatory synaptic boutons in layer 5 of the adult human temporal lobe neocortex: a fine-scale electron microscopic analysis. *Cereb Cortex*. 29:2797–2814.

Yakoubi R, Rollenhagen A, von Lehe M, Miller D, Walkenfort B, Hasenberg M, Sätzler K, Lübke JH. 2019b. Ultrastructural heterogeneity of layer 4 excitatory synaptic boutons in the adult human temporal lobe neocortex. *Elife*. 8:1–36.

Zhang ZW, Deschenes M. 1997. Intracortical axonal projections of lamina VI cells of the primary somatosensory cortex in the rat: a single-cell labeling study. *J Neurosci*. 17:6365–6379.

Zhang ZW, Deschenes M. 1998. Projections to layer VI of the posteromedial barrel field in the rat:a reappraisal of the role of corticothalamic pathways. *Cereb Cortex*. 8:428–436.

Zhang Z, Wu Y, Wang Z, Dunning FM, Rehfuss J, Ramanan D, Chapman ER, Jackson MB. 2011. Release mode of large and small dense -core vesicles specified by different synaptotagmin isoforms in PC12 cells. *Mol Biol Cell*. 22:2324–2336 https://doi.org/10.1091/mbc.e11-02-0159.

Zhang S, Xu M, Kamigaki T, Hoang Do JP, Chang WC, Jenvay S, Miyamichi K, Luo L, Dan Y. 2014. Selective attention. Long-range and local circuits for top-down modulation of visual cortex processing. *Science*. 345:660–665.

Zhao S, Studer D, Chai X, Graber W, Brose N, Nestel S, Young C, Rodriguez EP, Sätzler K, Frotscher M. 2012a. Structural plasticity of hippocampal mossy fiber synapses as revealed by high-pressure freezing. *J Comp Neurol*. 520:2340–2351.

Zhao S, Studer D, Chai X, Graber W, Brose N, Nestel S, Young C, Rodriguez EP, Saetzler K, Frotscher M. 2012b. Structural plasticity of spines at giant mossy fiber synapses. *Front Neural Circuits*. 6:103.

Zhou YD, Fuster JM. 1996. Mnemonic neuronal activity in somatosensory cortex. *Proc Natl Acad Sci U S A*. 93:10533–10537.

Zilles K, Bacha-Trams M, Palomero-Gallagher N, Amunts K, Friederici AD. 2015. Common molecular basis of the sentence comprehension network revealed by neurotransmitter receptor fingerprints. *Cortex*. 63:79–89.

Zilles K, Palomero-Gallagher N. 2017. Multiple transmitter receptors in regions and layers of the human cerebral cortex. *Front Neuroanat*. 11:78.